Conductive MeCbl/PEDOT:PSS/HA hydrogels with electrical stimulation for enhanced peripheral nerve regeneration

Kai Liu [a,d], Jiangbo Shao [c], Beibei Han [a,d], Jianfeng Liu [a,d], Shuai Yan [e], Bin Liu [a,d,**], Yao Liu [b,d,*]

[a] *Department of Hand and Foot Surgery, Orthopedics Center, The First Hospital of Jilin University, Changchun, 130021, China*
[b] *Department of Sport Medicine, Orthopedics Center, The First Hospital of Jilin University, Changchun, 130021, China*
[c] *Department of Ultrasound Diagnosis, The First Hospital of Jilin University, Changchun, Jilin, 130021, China*
[d] *Engineering Laboratory of Tissue Engineering Biomaterials of Jilin Province, Changchun, 130021, China*
[e] *Department of Operating Room, The First Hospital of Jilin University, Changchun, 130021, China*

A B S T R A C T

Peripheral nerve regeneration (PNR) represents a substantial challenge in the medical field, primarily due to the limited regenerative capacity of the peripheral nerve system (PNS). Current research efforts are focused on developing advanced medical polymer materials to enhance nerve recovery. Despite significant progress, several critical issues remain unresolved, including biocompatibility, stability, mechanical strength, controlled degradation rates, and sustained release of therapeutic agents. This study examines the utilization of hyaluronic acid hydrogels, doped with mecobalamin (MeCbl) and conductive poly(3,4-ethylenedioxythiophene):polystyrene sulfonate (PEDOT:PSS), in combination with exogenous electrical stimulation (ES) for PNR of rats. The strategy utilizes the MeCbl hydrogel to create a regenerative microenvironment and provide nutritional support for nerve cells, while PEDOT:PSS facilitates enhanced electrical signal conduction. ES has been shown to promote PNR and functional recovery, thereby demonstrating considerable potential. This study aims to comprehensively analyze the synergistic effects and potential value of this combined therapeutic approach, providing novel insights and pathways for the effective PNR.

1. Introduction

Peripheral nerve injury (PNI) refers to damage sustained by the nerve plexuses, trunks, or their branches within the peripheral nerve system (PNS), commonly resulting from lacerations, motor vehicle accidents, compression, or excessive stretching due to traumatic factors [1]. Repairing damaged peripheral nerves remains a significant clinical challenge. Current treatments, including direct suturing, autologous nerve grafting, and nerve guidance conduits (NGCs), are limited by functional recovery inefficiency, donor site morbidity, and inadequate replication of the native nerve microenvironment [2]. These limitations highlight the need for innovative strategies to enhance peripheral nerve regeneration (PNR).

With the advancement of tissue engineering, hydrogels have emerged as promising candidates for PNR due to their unique properties, such as high-water content, structural resemblance to the extracellular matrix, porosity, and excellent biocompatibility [3]. Their soft and elastic texture minimizes tissue irritation, while their three-dimensional (3D) porous structure supports cell adhesion, proliferation, and nutrient delivery, creating a favorable microenvironment for PNR [4]. However, conventional hydrogels often lack the necessary bioactivity and conductivity to fully support PNR, prompting the development of functionalized hydrogels [3].

Conductive hydrogels (CHs) have gained attention for their ability to mimic the electrophysiological properties of nerve tissue, facilitating nerve signal conduction and cell communication [5]. Additionally, incorporating neurotrophic agents, such as mecobalamin (MeCbl), into hydrogels can further enhance PNR by promoting neuronal cell growth [6]. Despite these advances, the development of multifunctional hydrogels that combine neurotrophic agents, conductive materials, and electrical stimulation (ES) for PNR remains a significant challenge, with limited studies exploring their full potential [7].

In this study, we developed an hyaluronic acid (HA) hydrogel functionalized with tannic acid (TA) to encapsulate MeCbl and poly(3,4-ethylenedioxythiophene):polystyrene sulfonate (PEDOT:PSS), creating a multifunctional platform for PNR. This hydrogel leverages the synergistic effects of ES, controlled drug release, and microenvironment modulation to enhance PNR in rats, as illustrated in Scheme 1. The results demonstrate that the combined approach significantly improves PNR, offering a simple yet effective strategy for nerve tissue engineering and PNI treatment.

2. Materials and methods

2.1. Materials

HA was purchased from Bloomage Biotechnology Corporation Limited (Jinan, P. R. China). 3-Aminophenylboronic acid (3-APBA) and N-hydroxysuccinimide (NHS) were purchased from Bide Pharmatech Co., Ltd. (Shanghai, P. R. China). 1-ethyl-3(3 dimethyl amino-propyl)-2-carbodiimide (EDC), TA, and MeCbl were purchased from Shanghai Aladdin Biochemical Technology Co., Ltd. (Shanghai, P. R. China). PEDOT:PSS, neurofilament-200 (NF200) antibody, and glial fibrillary acidic protein (GFAP) antibody were purchased from Sigma-Aldrich (Shanghai, P. R. China). S100 antibody, Synaptophysin (Syn) antibody, Neurofilament-L (NF-L) antibody, myosin heavy chain (MYH) 1 antibody, MYH7 antibody, CD11b antibody, and CD 68 antibody were purchased from Proteintech Group, Inc. (Wuhan, P. R. China). The rat Hematoxylin-eosin (H&E) kit, the Masson kit, the paraformaldehyde (PFA), and the Dulbecco's modified eagle medium (DMEM) were purchased from Servicebio Co., Ltd (Wuhan, P. R. China). Cell counting kit-8 (CCK-8) and Triton X-100 were purchased from Beyotime Biotechnology Co., Ltd (Shanghai, P. R. China). 4',6-diamidino-2-phenylindole (DAPI) was purchased from Solarbio Co., Ltd (Beijing, P. R. China). Clear tissue culture polystyrene (TCP) plates were purchased from Corning Costar Co., Ltd (Cambridge, MA, USA). The living/dead cell double staining kit was purchased from Bestbio Co., Ltd (Shanghai, P. R. China). Myelin basic protein (MBP) antibody and rat Schwann cells (SCs) were

purchased from Bihe Biochemical Technology Co., Ltd (Shanghai, P. R. China). Sprague-Dawley (SD) rats were purchased from the animal experiment center of Jilin University (Changchun, P. R. China). Bungarotoxin (BTX) was purchased from MedChemExpress LLC (Shanghai, P. R. China).

2.2. Exploration of the optimal concentration of PEDOT:PSS

In this study, we employed a gradient dilution method to determine the optimal concentration of PEDOT:PSS. A 96-well culture plate was used, with 50 wells arranged in a 5-row by 10-column format. Each well was inoculated with 5×10^3 SCs and 200 μL of culture medium and incubated for 24 h in a cell incubator (Thermo Fisher Scientific, Shanghai, P. R. China). After incubation, the culture medium was carefully aspirated from the wells.

For the first 5 wells in column 1, 100 μL of PEDOT:PSS solution was added and mixed thoroughly with 100 μL of fresh culture medium. A serial dilution was then performed by transferring 100 μL of the mixture from column 1 to column 2, mixing thoroughly, and repeating this process sequentially up to column 10. After the final transfer, 100 μL of the mixture from column 10 was discarded to maintain a consistent volume of 100 μL in each well. The plate was incubated for an additional 24 h.

Following incubation, the supernatant was aspirated and each well was replenished with a fresh mixture of CCK-8 reagent solution and culture medium. The plate was incubated until an orange color developed, indicating the presence of viable cells. Absorbance was measured using a Bio-Rad microplate reader (model 550, Hercules, California, USA). The same procedure was followed for experiments conducted at different time points or with different cell types. Groups co-incubated with PEDOT:PSS solution were designated as A (sample), groups cultured with medium containing only cells were set as A (control), and groups with plain culture medium were designated as A (blank). Cell viability was calculated using the following formula (1):
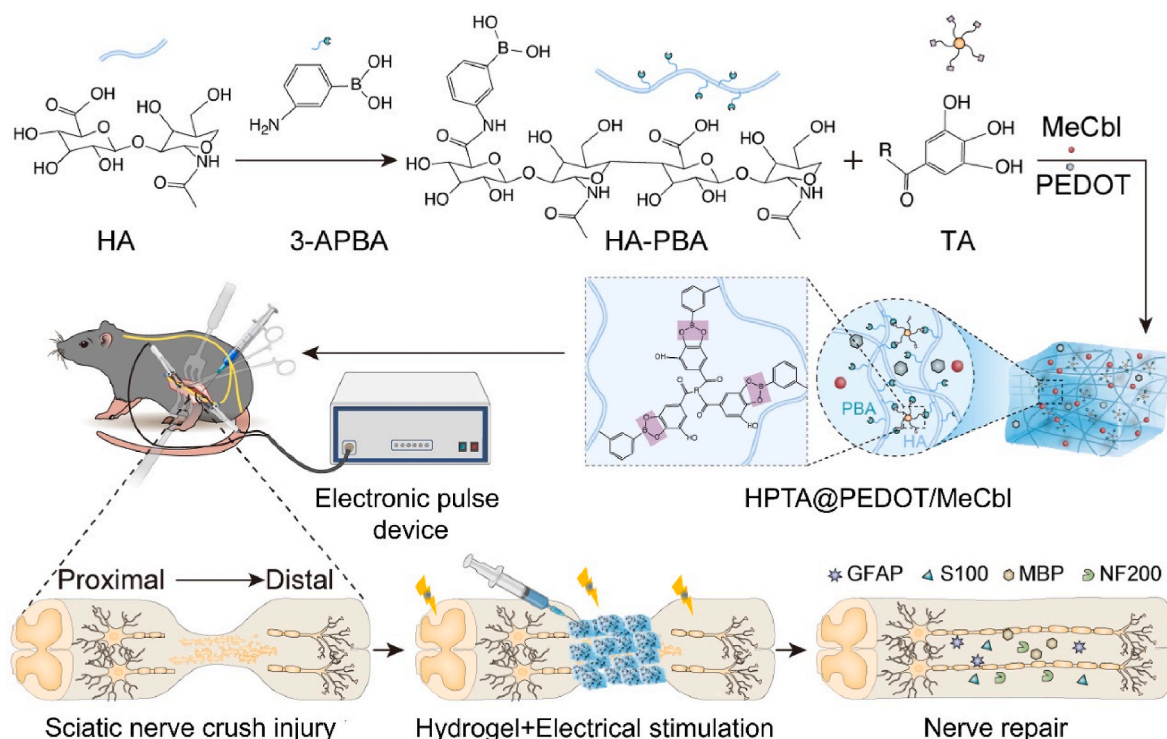
Scheme 1. Schematic representation of the integration of ES with conductive MeCbl/PEDOT/HA hydrogels for enhancing PNR.

$$\text{Cell viability (\%)} = \frac{A_{sample} - A_{blank}}{A_{control} - A_{blank}} \times 100\% \qquad (1)$$

2.3. Preparation and characterization of hydrogels

Based on previous research, this study successfully synthesized the conjugate of HA and 3-APBA through the chemical coupling of the carboxyl groups (-COOH) on HA with the amino groups (-NH$_2$) on 3-APBA, yielding the conjugate HA-PBA [8]. The experimental procedure is as follows: Initially, 3 g of HA was dissolved in 300 mL of deionized water, and the pH of the solution was adjusted to 6.0 using 0.1 M hydrochloric acid (HCl). Subsequently, EDC·HCl (1.34 g) and NHS (0.86 g) were added at a molar ratio of 1:1 relative to HA. The mixture was stirred at room temperature for 1 h to ensure complete dissolution of any precipitates or particles. Finally, 1 g of 3-APBA was added at a molar ratio of 3:1 relative to the -COOH groups of HA, and stirring was continued. The reaction mixture was stirred at ambient temperature for 72 h to ensure efficient conjugation. The resultant solution was transferred into a dialysis bag with a molecular weight cutoff of 14 kDa and dialyzed against deionized water for 3–4 d, with water exchanges performed 2 to 3 times daily. The dialyzed solution was then lyophilized using a freeze-dryer (Xinzhi Biotechnology Co., Ltd., Zhejiang, P.R. China) for 3 d to obtain the HA-PBA conjugate. The product was sealed and stored in a desiccator at room temperature for future use.

A 2.5 wt% solution of HA-PBA was thoroughly mixed with a 9 wt% solution of TA using a vortex mixer (MV-100, Servicebio Co., Ltd., Wuhan, P.R. China) to form the HPTA hydrogel. To prepare hydrogels loaded with MeCbl and/or PEDOT:PSS, the HA-PBA solution was mixed with the MeCbl solution. Subsequently, the PEDOT:PSS solution and TA solution were combined using a vortex mixer to produce HPTA/MeCbl, HPTA/PEDOT:PSS, and HPTA/PEDOT:PSS/MeCbl hydrogels. For clarity in subsequent descriptions, the conductive hydrogels HPTA/PEDOT:PSS and HPTA/PEDOT:PSS/MeCbl are referred to as CHs and CHs/MeCbl, respectively. The specific compositions of the hydrogels utilized in this study are detailed in Table 1.

The gelation properties of the hydrogel were evaluated using the inverted bottle method. Lyophilized hydrogel samples were rapidly frozen in liquid nitrogen, sectioned to expose their internal structure, and subjected to gold-palladium sputtering treatment. The micromorphology and network structure were examined using a scanning electron microscope (SEM, Inspect-F, FEI, Hillsboro, USA). Rheological characterization, including frequency sweeps, stress-strain analysis, shear thinning behavior, and self-healing capability assessments, was performed using a rheometer (Anton Paar, Graz, Austria). The electrical conductivity of the hydrogel was assessed using an electrical multimeter (DELIXI ELECTRIC Co., Ltd., Anhui, P. R. China). The self-healing capability of the hydrogel was evaluated by making an incision on the hydrogel placed on the dorsal side of a finger and assessing its healing through finger flexion and extension movements. The injectability was confirmed by injecting the hydrogel into the phosphate-buffered saline (PBS) solution and forming English letters. Adhesiveness was evaluated by placing the hydrogel between two glass slides and allowing it to remain in place for 30 min. The bonding strength of the hydrogel bridging the two glass slides was measured using a universal testing machine (Shimadzu, Kyoto, Japan) at a stretching rate of 20 mm/min,

with the breaking force recorded as F. The overlapping area between the two glass slides was designated as S. The adhesive force of the hydrogel was calculated using the following formula (2):

$$\text{Adhesion strengths (Pa)} = \frac{F}{S} \qquad (2)$$

where F was in "N", and S was in "m^2".

To evaluate the release profile of MeCbl, the hydrogel was immersed in 40 mL of PBS and incubated in a 37 °C constant temperature shaker (Yineng Laboratory Instruments Factory, Jiangsu, P. R. China). At predetermined time intervals, 1 mL of the release medium was withdrawn and immediately replaced with 1 mL of fresh PBS. The characteristic absorption peak of MeCbl at a wavelength of 350 nm was measured using an Ultra-Violet spectrophotometer (UVS, LAMBDA, NJ, USA) to obtain the optical density (OD) values of the release solution. The release amount of MeCbl at various time points was determined by substituting the OD values into the standard curve equation for MeCbl. To assess the degradation rate, a hydrogel sample with an initial mass of W$_0$ was immersed in 1 mL of PBS. At predetermined intervals, the PBS was replaced, and each hydrogel sample was weighed (W$_t$). The degradation rate of the hydrogel was calculated using formula (3):

$$\text{Mass remaining (\%)} = \frac{W_t}{W_0} \times 100\% \qquad (3)$$

where M$_t$ and W$_0$ were in "g".

2.4. Free radical scavenging assay of hydrogels

In this study, the scavenging capability of hydrogels against 2,2-diphenyl-1-picrylhydrazyl-hydrate (DPPH•) radicals was assessed using an established method [9]. Initially, 10 mg of DPPH• was dissolved in 50 mL of methanol and subjected to ultrasonication for 20 min to prepare the DPPH• solution. The CHs/MeCbl hydrogel samples were divided into 5 groups based on a mass gradient (20 mg, 10 mg, 5 mg, 2.5 mg, and 1.25 mg). Equivalent masses of TA samples were prepared in centrifuge tubes. After adding 1 mL of DPPH• solution to each sample, the mixtures were incubated at 37 °C for 30 min. Subsequently, 100 μL aliquots of the solutions were transferred to a 96-well plate, and the OD at 517 nm was measured under light-protected conditions using a microplate reader (Bio-Rad 550, Hercules, California, USA). The DPPH• solution without hydrogel or TA served as the control group (A control), while the DPPH• solution co-incubated with the hydrogel was designated as the experimental group (A sample). The scavenging efficiency of DPPH• radicals was calculated using formula (4):

$$\text{Scavenging effect (\%)} = \frac{A_{control} - A_{sample}}{A_{control}} \times 100\% \qquad (4)$$

Following the methodologies outlined in the literature, this study also evaluated the scavenging efficacy of CHs/MeCbl hydrogel against 2-Phenyl-4,4,5,5-tetramethylimidazoline-1-oxyl 3-Oxide (PTIO•) radicals [10]. Specifically, 14 mg of PTIO• was dissolved in 40 mL of deionized water. The prepared CHs/MeCbl hydrogel was allocated into 5 distinct groups based on a mass gradient (20 mg, 10 mg, 5 mg, 2.5 mg, and 1.25 mg). For each group, an equivalent mass of TA was introduced into 1 mL of the PTIO• solution. After incubation in a 37 °C incubator for 2 h, 100 μL of each solution was transferred to a 96-well plate. The OD value at 557 nm was measured using a microplate reader. The PTIO• solution without hydrogel and TA served as the control group (A control), while the PTIO• solution co-incubated with the hydrogel was designated as the experimental group (A sample). The scavenging efficiency of PTIO• radicals was calculated using formula (4).

2.5. Effects of hydrogels on cell behavior

The hydrogel was uniformly coated on the bottom of 6-well plates.

Table 1
Formulation ratios of hydrogels.

Hydrogel	HA-PBA (mg)	TA (mg)	MeCbl (mg)	PEDOT:PSS (%)	PBS (mL)
HPTA	10	9	–	–	0.5
HPTA/ MeCbl	10	9	5	–	0.5
CHs	10	9	–	0.016	0.5
CHs/MeCbl	10	9	5	0.016	0.5

Rat SCs and human umbilical vein endothelial cells (HUVECs) were then seeded onto the hydrogel surface. After 24 h of cell culture, the cells were then subjected to ES at 150 mV/mm using a 9130B triple-output programmable direct current (DC) power supply (B&K Precision, CA, USA) for 6 h, followed by cell live/dead staining experiment.

The schematic diagram of the DC power supply applied ES to cells is shown in Fig. S1A. After adjusting the parameters of the power supply, the ES module delivers ES to the cells in the 6-well plate (Figs. S1B and C). The sterilized ES module can be placed inside the cell culture incubator, and the red and black electrode wires are connected to the external power supply through a sealed port at the back of the incubator. This power supply enables ES to be applied to the cells in the 6-well plate under standard cell culture conditions, thereby enhancing cell proliferation. The ES parameters for the cell experiments were selected based on previous studies and further optimized for our experimental conditions [11,12].

Calcein AM and propidium iodide (PI) fluorescent dyes were prepared. After removing the culture medium from the wells, staining was conducted under light-protected conditions for 30 min. Observations and documentation were performed using a fluorescence microscope (IX73, Olympus, Tokyo, Japan). Calcein AM fluorescence was used to identify viable cells (green), while PI fluorescence indicated dead cells (red) [13].

To examine the impact of hydrogels on the hemolysis rate of rat red blood cells, we isolated rat red blood cells by centrifugation and washed them with PBS to prepare a 2 % (v/v) red blood cell suspension. The hydrogel was co-incubated with this suspension at 37 °C for 2 h. Both the experimental group and the blank control group (2 % v/v red blood cell PBS suspension), as well as the positive control group (2 % v/v red blood cell ultrapure water suspension), were processed according to this protocol. After incubation, 100 μL of the supernatant from each sample was transferred to a 96-well plate, and the OD at 576 nm was measured using a microplate reader. The hemolysis rate was calculated using formula (5):

$$\text{Hemolysis rate } (\%) = \frac{\text{OD}_{\text{experiment group}} - \text{OD}_{\text{blank group}}}{\text{OD}_{\text{positive group}} - \text{OD}_{\text{blank group}}} \times 100\% \quad (5)$$

For cell viability assays, 100 μL of the hydrogel extract was added to each well of a 96-well plate, ensuring a cell density of 8×10^3 cells per well for SCs. The plate was incubated for 24 h. After incubation, the extract was aspirated, and CCK-8 reagent solution was added. The plate was then incubated at 37 °C for 40 min until an orange-yellow color developed. The OD was measured at 450 nm using a microplate reader, and cell viability was calculated using formula (1).

The reactive oxygen species (ROS) scavenging efficacy of the hydrogels against H_2O_2-induced intracellular ROS was evaluated using the 2′,7′-dichlorodihydrofluorescein diacetate (DCFH-DA) staining assay. Sample extracts were prepared by co-incubating the hydrogels or TA with DMEM culture medium supplemented with 500 μM H_2O_2 for 24 h. SCs were seeded in 12-well plates and cultured for 24 h. After this initial incubation, the culture medium was replaced with sample extracts, and the cells were further incubated for 6 h. The cells were then washed with PBS and incubated with DCFH-DA solution for 30 min. Fluorescence microscopy was used to observe the cells, and fluorescence images were quantitatively analyzed using the ImageJ software (National Institutes of Health, http://rsb.info.nih.gov/ij/).

2.6. Degradation of hydrogels in vivo

The degradation characteristics of the hydrogels were evaluated *in vivo* using the SD rat model. Female SD rats, aged 4–6 weeks and weighing 180–220 g, were obtained from the animal experiment center of Jilin university. Following a 1-week acclimation period to the new environment, the rats underwent surgical procedures. The animals were placed in a prone posture, and 0.5 mL of hydrogel was injected into the interspace between the dorsal skin and subcutaneous muscle using a syringe. At predetermined time points, the rats were euthanized, and the degradation process of the hydrogel was observed and documented. To assess the biocompatibility of the hydrogel, tissue samples from the subcutaneous region covered by the hydrogel were collected and subjected to H&E staining. The stained sections were examined, imaged, and analyzed using a fluorescence microscope.

2.7. Procedures of animal experimentation

In this study, animals were randomly allocated into 4 groups, each comprising 5 rats: the sciatic nerve crush group (Crush group), the ES group, the ES combined with CHs group (ES + CHs group), and the ES combined with CHs/MeCbl group (ES + CHs/MeCbl group). All rats underwent left sciatic nerve crush surgery under anesthesia [14].

During the procedure, the rats were positioned in right lateral recumbency, and a 3 cm skin incision was made posterior to the left femur. The gluteal muscles were carefully dissected to expose the sciatic nerve. A hemostat was used to crush the sciatic nerve for 1 min. In the Crush group, only the nerve crush procedure was performed. In contrast, the ES group underwent ES treatment following the nerve crush using an electronic pulse generator (Suzhou Medical Supplies Factory Co., Ltd, Jiangsu, P. R. China). The stimulation parameters were set at a frequency of 20 Hz, a duty cycle of 50 %, and a working voltage of 100 mV, with platinum wire electrodes positioned both proximally and distally to the nerve. Each stimulation session lasted for 2 h and was administered once every other day for a total of 5 treatments (Fig. S1D). The treatment parameters were based on those previously established by our research team and reported in relevant literature. Studies have demonstrated that ES with these parameters effectively promotes nerve regeneration in the lower limbs of rats [15,16].

All groups underwent 8-0 suture placement at the proximal site of the sciatic nerve injury. Following muscle and skin closure, the animals were returned to their cages for further experimentation. Postoperatively, each rat received intramuscular penicillin injections to prevent infection. To minimize the risk of wound biting and infection, all postoperative rats were housed individually for at least 1 week. All surgical procedures were conducted by the same surgeon to ensure procedural consistency.

2.8. Analysis of walking tracks

At 4 weeks postoperatively, the recovery of motor function in rats was evaluated using the MGT-PR rodent gait analysis system (Zhenghua Biologic Apparatus Facilities Co., Ltd., Anhui, P. R. China) [19]. Before testing, the transparent glass walking track was cleaned with water or alcohol to ensure clear visibility. The hind paws of the rats were moistened to facilitate the recording of footprints. Each rat was then guided to walk from one end of the track to the other, during which the gait patterns were captured by a camera positioned beneath the track. Footprint data were collected to obtain the following parameters: intermediary toe (IT) spread, toe spread (TS), and paw length (PL). The sciatic functional index (SFI) was subsequently calculated using formula (6) [17]:

$$SFI = \frac{-38.3 \times (EPL - NPL)}{NPL} + \frac{109.5 \times (ETS - NTS)}{NTS}$$
$$+ \frac{13.3 \times (EIT - NIT)}{NIT} - 8.8 \quad (6)$$

where E is the injured side (left side), and N is the normal side (right side).

2.9. Electrophysiological analysis, histological evaluation, and immunofluorescence examination of the sciatic nerve

At 4 weeks post-treatment, the bilateral compound muscle action

potentials (CMAPs) of the lower extremities in rats were recorded using a 9033A07 EMG/evoked potentiometer (Bendi Medical Equipment Co., Ltd, Shanghai, China). Before testing, the equipment was calibrated, and the electrodes were sterilized. Rats were anesthetized with pentobarbital sodium, and bilateral sciatic nerves were surgically exposed through small incisions in the thigh regions. Stimulating electrodes were placed at the proximal end of each sciatic nerve, while recording electrodes were inserted into the belly of the gastrocnemius muscle (GM) on each side. A ground electrode was positioned near the base of the tail. A single square-wave pulse was delivered to evoke CMAPs, and the responses were recorded. Each measurement was repeated 3 times on both sides to ensure consistency. The amplitude and latency of the CMAPs were analyzed to evaluate PNR and functional recovery.

For histological evaluation, sections of the regenerated nerves were prepared for H&E staining and toluidine blue (TB) staining. The diameter of the regenerated nerve fibers and the thickness of the myelin sheaths were characterized using a transmission electron microscope (TEM, HT7800/HT7700, hitachi, Japan). The diameters of the regenerated nerve fibers and the myelin sheath thickness were quantified using the Nano-Measurer software based on the image results. Immunofluorescence staining for NF200, MBP, GFAP, and S100 was performed to detect neural axon regeneration. Images were acquired using a confocal laser scanning microscope (CLSM, AXR(Ti2-E), Nikon, Japan). The immunofluorescence results of the regenerated nerves were analyzed using the ImageJ software.

2.10. Histological and immunofluorescence examination of GM, extensor digitorum longus (EDL), and motor endplate (MEP)

At 4 weeks post-treatment, we assessed the histopathology of GM and EDL specimens from rats. The bilateral GMs and EDLs were weighed, and the percentage of bilateral muscle weight was calculated using equation (7):

$$Weight\ (\%) = \frac{Weight\ (E)}{Weight\ (N)} \tag{7}$$

Weight (E) and Weight (N) denoted the muscle weight of the GM and EDL on the experimental and normal sides, respectively.

Paraffin sections of the GM and EDL were subjected to Masson's trichrome staining as well as fast and slow myofiber-specific staining. Fluorescence microscopy was used to acquire images of the stained sections, while CLSM was employed to capture detailed images of muscle fibers. The number, diameter, and cross-sectional area of the muscle fibers were quantitatively analyzed using ImageJ software. Immunofluorescence staining of GM and EDL fibers was performed using antibodies against BTX, Syn, and NF-L. CLSM was used to acquire images, followed by quantitative analysis of MEP parameters, including diameter, circumference, area, and fragmentation rate. To evaluate the biocompatibility of the hydrogel, paraffin sections were prepared from both muscle types after hydrogel injection, and immunohistochemical staining for CD11b and CD68 was conducted.

2.11. Transcriptomic assay of the regenerated sciatic nerve

The animal tissue specimens were cryopreserved at −80 °C immediately after isolation to ensure optimal preservation. RNA integrity was evaluated using the Bioanalyzer 2100 system with the RNA nano 6000 assay kit. Total RNA was used as input material for the preparation of RNA samples. The index-coded samples were clustered on a cBot cluster generation system using the TruSeq PE Cluster Kit v3-cBot-HS (Illumia), following the manufacturer's instructions. After cluster generation, the library preparations were sequenced on an Illumina Novaseq platform, generating 150 bp paired-end reads. The raw data in fastq format were initially processed using fastp software. Reference genome and gene model annotation files were directly downloaded from the genome

website. The mapped reads for each sample were assembled using StringTie (v1.3.3b) in a reference-based approach [18]. The number of reads mapped to each gene was quantified using FeatureCounts v1.5.0-p3.

Gene ontology (GO) enrichment analysis of differentially expressed genes (DEGs) was performed using the clusterProfiler package, with gene length bias correction applied. GO terms with corrected P-values less than 0.05 were considered significantly enriched by DEGs. The kyoto encyclopedia of genes and genomes (KEGG) serves as a database resource for understanding high-level functions and utilities of biological systems, including cells, organisms, and ecosystems, based on molecular-level information derived from large-scale molecular datasets generated through genome sequencing and other high-throughput experimental technologies (http://www.genome.jp/kegg/). The clusterProfiler package was also used to assess the statistical enrichment of DEGs in KEGG pathways. Gene set enrichment analysis (GSEA) is a computational method used to determine whether a predefined gene set exhibits significant and consistent differences between two biological states. The GSEA analysis tool (http://www.broadinstitute.org/gsea/index.jsp), along with GO and KEGG datasets, was independently employed for conducting GSEA.

2.12. Evaluation of nutritional status and assessment of organ toxicity in rats

The nutritional status of rats was evaluated by analyzing changes in body weight over 4 weeks. Specimens of the heart, liver, spleen, lungs, and kidneys were prepared as paraffin sections and subjected to H&E staining. Microscopic images were captured for subsequent analysis.

2.13. Statistical analysis

Data were presented as the mean ± standard deviation (SD) and were analyzed with the GraphPad Prism 9.5.0 software (Graphpad Inc., San Diego, CA, USA). The Student's t-test was used for statistical analysis. Statistical significance was set at $*P < 0.05$ and high statistical significance was set as $**P < 0.01$ and $***P < 0.001$.

3. Results and discussion

3.1. Exploring the optimal concentration of PEDOT:PSS solution

This study investigated the effects of different concentrations of PEDOT:PSS solution on cell viability. The results demonstrated that high concentrations of PEDOT:PSS significantly inhibited cell viability, whereas appropriately diluted solutions markedly enhanced cell viability. A gradient dilution of the PEDOT:PSS solution was performed using PBS (Fig. 1A). At a concentration of 0.5 %, the diluted PEDOT:PSS solution exhibited no significant change in color. When the concentration was reduced to 0.016 %, the solution's color gradually lightened and approached transparency. We further evaluated the impact of varying concentrations of PEDOT:PSS solution on the viability of SCs and HUVECs. Cell viability at multiple time points was assessed using the CCK-8 assay kit (Fig. 1B). Following a 24-h incubation period, even at a concentration as low as 0.125 %, the PEDOT:PSS solution significantly inhibited SCs viability. However, when the concentration was decreased to 0.063 %, cell viability showed marked improvement, although a residual inhibitory effect was still observed.

At a concentration of 0.032 %, cell viability was significantly enhanced. Further dilution did not result in substantial differences in cell viability between adjacent concentrations; however, the overall trend indicated that as the PEDOT:PSS solution was diluted, cell viability gradually increased, reaching a peak before declining. Both SCs and HUVECs exhibited similar patterns of change in viability at the 48-h and 72-h time points. This phenomenon may be attributed to the osmotic pressure effects and cytotoxicity associated with high-concentration
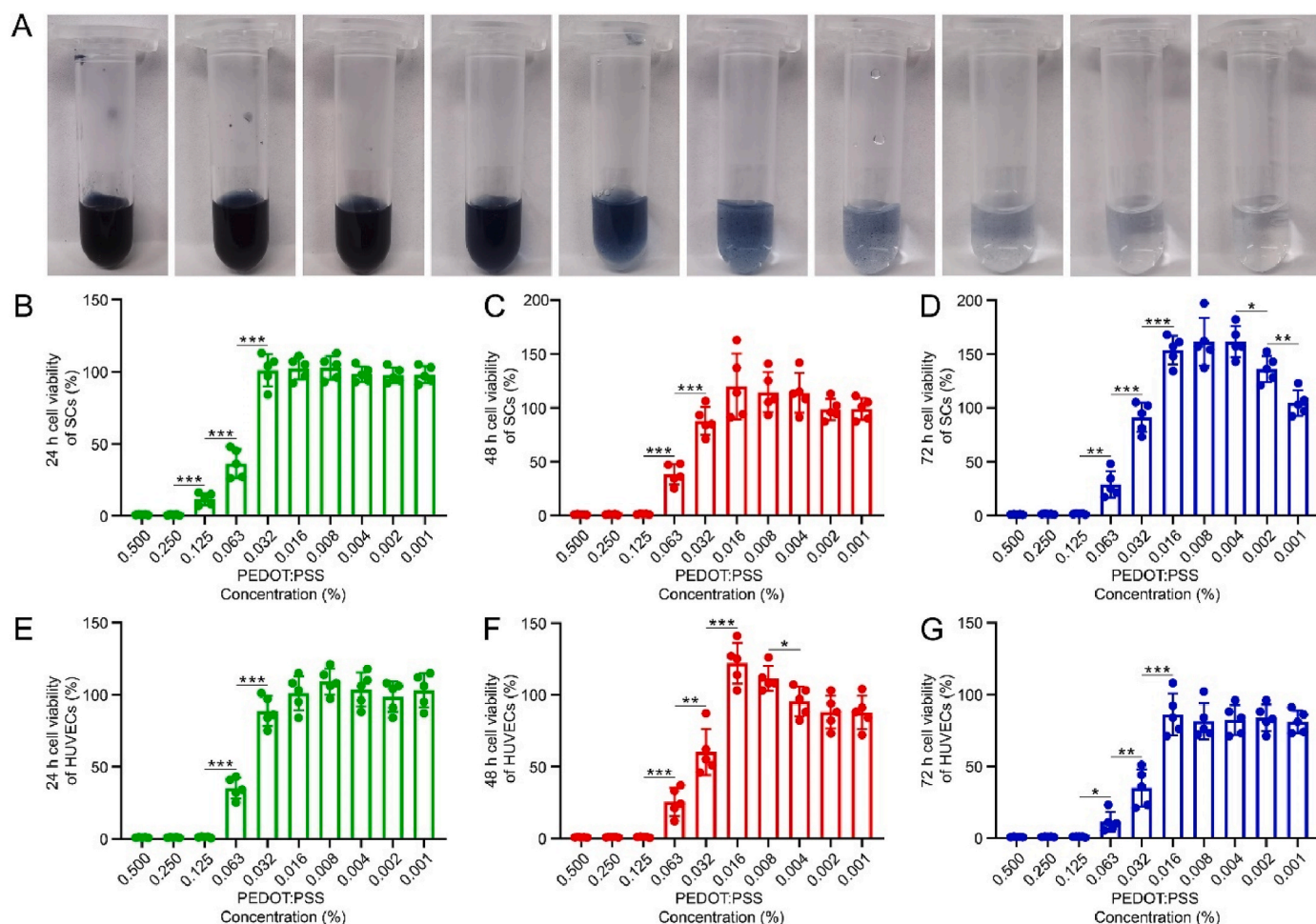
Fig. 1. The impact of gradient dilution of the PEDOT:PSS solution on cell proliferation. (**A**) The external appearance of the gradient dilution of the PEDOT:PSS solution. (**B**) The effect of gradient dilution of the PEDOT:PSS solution on the proliferation of SCs and HUVECs (n = 5, n represents the number of experimental replicates at each coating concentration). All statistical data are represented as mean ± SD (* indicates P < 0.05, ** indicates P < 0.01, *** indicates P < 0.001).

solutions, which inhibit cell growth. Conversely, appropriate dilution of PEDOT:PSS, owing to its hydrophilicity and conductivity, enhances cell adhesion and proliferation [19]. Conductive polymers (CPs) have the potential to modulate the electric field in cell membranes, thereby influencing ion channels and bioelectric activities within the membrane, which can promote cell growth [20]. By integrating experimental data from 6 distinct time points, it was determined that a concentration of 0.016 % is optimal for sustaining cell growth. Consequently, this concentration was chosen for the preparation of the conductive hydrogel.

The impact of varying concentrations of PEDOT:PSS on the viability of SCs and HUVECs is substantial and demonstrates a concentration-dependent effect. Research has shown that low concentrations of PEDOT:PSS may enhance the proliferation of neural stem cells by activating voltage-gated calcium channels in the cell membrane [21]. This mechanism is comparable to ES, which can modulate intracellular calcium dynamics, thereby influencing the expression of cell cycle-related proteins and promoting cell cycle progression [19]. For HUVECs, the role of PEDOT:PSS may involve the upregulation of angiogenesis-related signaling pathways and the expression of associated proteins and cellular signaling factors, which are central to the proliferation and migration of vascular endothelial cells [22]. However, high concentrations of PEDOT:PSS may inhibit cell growth due to oxidative stress and cytotoxicity [23]. Consequently, the concentration of PEDOT:PSS is a critical factor in modulating its effects on cell viability, providing an important theoretical foundation for the design of CHs with specific bioactivity.

3.2. Synthesis and characterization of hydrogels

The gelation properties of the prepared hydrogels were evaluated using the inverted vial method, as illustrated in Fig. 2A. SEM was used to characterize the microstructural features of the hydrogels. As shown in Fig. 2B, the cross-sectional view of the hydrogel reveals an interconnected porous network, which facilitates efficient substance exchange. In the higher magnification images, crystalline deposits of MeCbl and PEDOT:PSS within the hydrogel matrix are discernible and exhibit uniform distribution throughout the network. These findings confirm that MeCbl and PEDOT:PSS are homogeneously dispersed within the HPTA hydrogel, thereby validating its suitability as a delivery vehicle for these compounds.

Under 1 % strain conditions, our rheological tests demonstrated that both hydrogels maintained a storage modulus (G′) higher than the loss modulus (G″) throughout the stable phase. However, with increasing stress and strain, G′ gradually decreased until it intersected with G''. Beyond this critical point, G′ fell below G″, indicating the disruption of the boronate ester bonds and the subsequent collapse of the hydrogel's network structure (Fig. 2C). All hydrogels exhibited a storage modulus (G′) exceeding 500 Pa, with values consistently higher than their corresponding loss moduli (G″). This mechanical profile, comparable to the strength range of native nerve tissue (100–1000 Pa), providing an optimal balance between flexibility and mechanical support for axonal extension [24]. Frequency sweep analysis at 1 % strain demonstrated that all 4 hydrogel formulations exhibited storage modulus (G′)
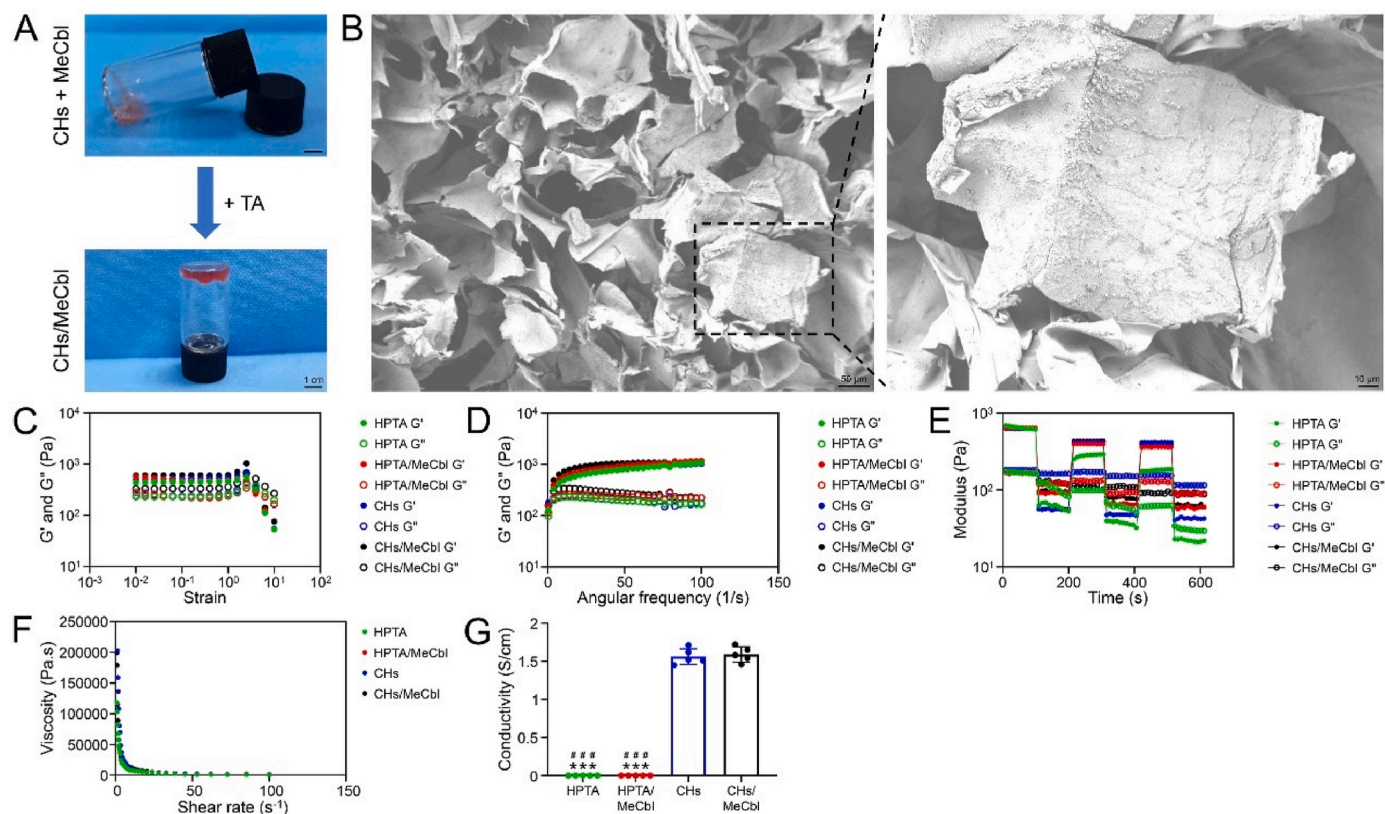
Fig. 2. Synthesis, microstructure, rheological properties, and electrical conductivity of hydrogels. (**A**) Gelation behavior of hydrogels evaluated by the inverted bottle method. (**B**) Microstructural analysis of hydrogels characterized by SEM. (**C**) Stress-dependent variations in storage modulus (G′) and loss modulus (G″) for 4 hydrogel formulations. (**D**) Frequency-dependent rheological properties of 4 hydrogel formulations. (**E**) Time-dependent evolution of G′ and G″ of 4 hydrogel formulations under cyclic strain conditions. (**F**) Shear rate-dependent viscosity behavior of 4 hydrogel formulations. (**G**) Electrical conductivity of 4 hydrogel formulations (n = 5, n indicates the number of samples tested in each group; *** indicates P < 0.001 compared with CHs group; ### indicates P < 0.001 compared with CHs/MeCbl group). All statistical data are represented as mean ± SD.

consistently exceeding loss modulus (G″) throughout the tested frequency range (Fig. 2D). Furthermore, the frequency-dependent viscoelastic behavior observed in all hydrogels suggests stable network structures with excellent mechanical integrity.

For self-healing characterization, the hydrogels were subjected to alternating strain conditions of 1 % and 600 %. As shown in Fig. 2E, under low strain conditions (1 %), the gel network maintained structural stability (G′ > G″). In contrast, application of high strain (600 %) resulted in disruption of the boronate ester bonds, transitioning the material to a sol state (G″ > G′). Remarkably, upon returning to 1 % strain, the hydrogel rapidly recovered its original modulus (G′ > G″). This recovery process was consistently observed over 3 cycles of alternating high and low strain. These findings indicate that the hydrogels can reliably transition between gel and sol states under cyclic strain conditions, thereby demonstrating superior self-healing capabilities. The injectability of the hydrogels was evaluated by shear rate testing. All hydrogels demonstrated a reduction in shear viscosity under increasing shear stress, which could be attributed to the disruption of their internal cross-linking structures. The test results were consistent across all samples, indicating that there were no significant differences in the injectability among the hydrogels (Fig. 2F).

We systematically investigated the electrical conductivities of 4 distinct hydrogel formulations (Fig. 2G). The intrinsic conductivity of the HPTA hydrogel, based on its hyaluronic acid matrix, was measured at $(1.1 \pm 0.4) \times 10^{-3}$ S/cm. This relatively low conductivity can be attributed to the lack of efficient electron transport pathways between HA molecules. The incorporation of MeCbl into the HPTA hydrogel resulted in a comparable conductivity of $(0.9 \pm 0.3) \times 10^{-3}$ S/cm, indicating that MeCbl molecules did not significantly contribute to

electronic conduction. In contrast, both CHs and CHs/MeCbl hydrogels exhibited substantially enhanced conductivities of 1.56 ± 0.09 S/cm and 1.59 ± 0.09 S/cm, respectively. This remarkable improvement, approximately 3 orders of magnitude higher than the HPTA hydrogels, is primarily attributed to the incorporation of PEDOT:PSS. CPs facilitates the establishment of an efficient electron transport network within the hydrogel matrix, thereby significantly optimizing the overall electrical performance.

The adhesive properties of the hydrogels were evaluated as shown in Fig. 3A. The shear adhesive strengths of the HPTA@MeCbl, CHs, and CHs/MeCbl hydrogels were measured at 50.17 ± 2.69 kPa, 51.25 ± 1.92 kPa, and 50.85 ± 3.55 kPa, respectively, which were not statistically different from that of the HPTA hydrogel at 50.67 ± 4.01 kPa (Fig. 3B). These results suggest that the incorporation of both MeCbl and PEDOT:PSS did not substantially interfere with the formation of hydrogen bonds and boronic ester bonds, which are crucial for maintaining the hydrogel's adhesive characteristics.

The degradability of implantable medical materials represents a crucial characteristic for minimizing patient trauma by eliminating the need for additional removal surgeries [25]. The degradation studies *in vitro* revealed that all 4 hydrogel formulations exhibited significant water absorption during the initial 3 days. Subsequent degradation in PBS solution showed varying patterns (Fig. 3C). By day 11, the residual mass of the hydrogels ranged from 40.7 % to 45.4 % of their initial mass, demonstrating comparable biodegradation rates without significant differences among formulations. These findings align with previous studies indicating that hydrogel degradation is predominantly influenced by crosslinking density [26], while the incorporation of MeCbl and PEDOT:PSS showed negligible effects on degradation kinetics.
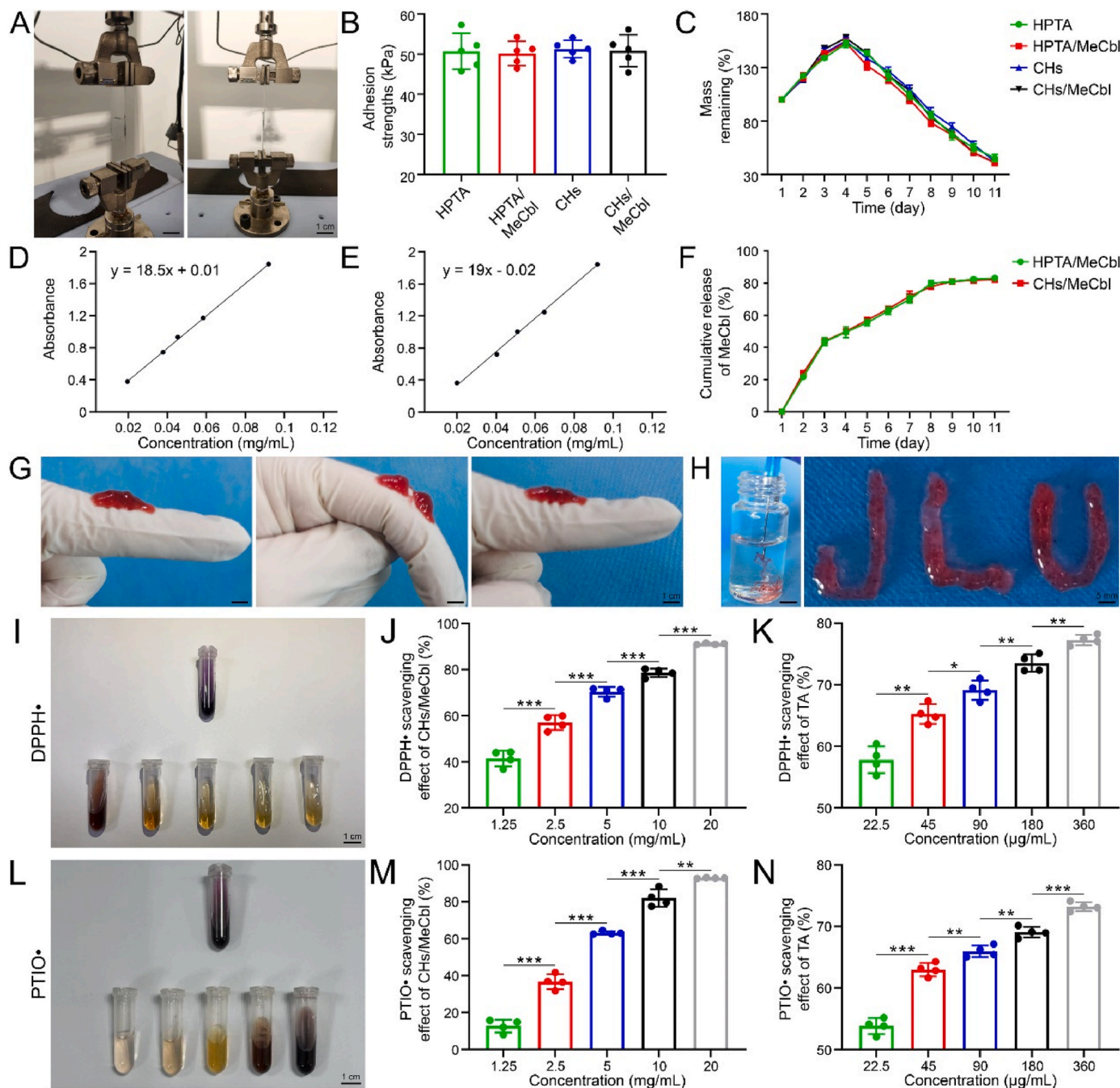
Fig. 3. Comprehensive characterization of hydrogel properties including physicochemical characteristics, degradation, drug release behavior, and antioxidant activity *in vitro*. (A) The adhesion testing performed using a universal testing machine. **(B)** Quantitative comparison of shear adhesive strength among different hydrogel groups ($n = 5$, n represents the number of samples tested in each group). **(C)** The degradation profiles *in vitro* of 4 hydrogel formulations ($n = 3$, n represents the number of samples tested in each group). **(D and E)** The standard curves for the MeCbl-loaded hydrogels were derived from the characteristic absorption peak of MeCbl at 350 nm. **(F)** The release kinetics of MeCbl ($n = 3$, n represents the number of samples tested in each group). **(G)** Demonstration of hydrogel's self-healing properties through sequential images showing adhesion, fracture, and re-healing on a finger surface. **(H)** Evaluation of injectability through 3 representative tests: extrusion into PBS solution, needle injection, and surface writing on glass substrate. **(I and L)** The color changes upon the addition of different concentrations of CHs/MeCbl to the DPPH• and PTIO• solutions, respectively. **(J and M)** Quantitative analysis of DPPH• and PTIO• radical scavenging rates by CHs/MeCbl hydrogel ($n = 4$, n indicates the number of experimental replicates). **(K and N)** The radical scavenging capacity of TA ($n = 4$, n indicates the number of experimental replicates). All statistical data are represented as mean $\pm$ SD (* indicates $P < 0.05$, ** indicates $P < 0.01$, *** indicates $P < 0.001$).

Before conducting the release experiments *in vitro* of HPTA@MeCbl and CHs/MeCbl hydrogels, we established the standard curve for MeCbl. By measuring the ultraviolet characteristic absorption peak at 350 nm for both hydrogels, we derived their respective linear regression equations: for the HPTA@MeCbl hydrogel, the equation was $y = 18.5x + 0.01$; and for the CHs/MeCbl hydrogel, the equation was $y = 19x - 0.02$

(Fig. 3D and E). These standard curves demonstrated excellent linearity within the concentration range of 0.02–0.1 mg/mL.

Release kinetics analysis revealed a biphasic profile: the rapid release during the initial 6 days followed by the sustained release from day 6 to day 11 (Fig. 3F). This release pattern likely results from the initial burst release of surface-associated MeCbl followed by diffusion-controlled

release from the hydrogel matrix. The similar release profiles between both hydrogel formulations suggest that PEDOT:PSS incorporation does not significantly alter the porous structure of the hydrogels, consistent with previous research [27]. Given MeCbl's well-documented roles in neurocyte proliferation, neuronal protection, myelin maintenance, and axonal regeneration [28], these release profiles are anticipated to achieve therapeutic concentrations for effective PNR.

Previous studies have shown that MeCbl concentrations ranging from 100 nM to 100 μM significantly enhance neurite outgrowth *in vitro* [29]. In our study, 5 mg of MeCbl was loaded into a hydrogel with a total volume of 500 μL, resulting in an initial MeCbl concentration of 7.44 mM within the hydrogel. While this concentration may appear high, it is important to note that the effective concentration of MeCbl in the local tissue environment is significantly lower due to the controlled release properties of the hydrogel. The release profile of MeCbl from the hydrogel was measured (Fig. S2). During the first 2 days, the cumulative release concentration of MeCbl exceeded 100 μM. However, the actual effective concentration acting on nerve cells is likely much lower than the release concentration due to factors such as dilution, diffusion, and metabolism in the local tissue microenvironment. Only a fraction of the released MeCbl reaches the target cells and exerts its biological effects.

Macroscopic evaluations demonstrated the hydrogel's self-healing and injectable properties. When applied to an extended finger and subjected to bending stress, the hydrogel fractured but completely fused within 10 min upon stress removal (Fig. 3G). Injectability tests showed that the hydrogel could be smoothly extruded through a syringe needle, maintaining structural integrity in PBS solution and demonstrating precise patterning capability on the glass surface (Fig. 3H). These

properties were consistent across all hydrogel formulations, indicating that MeCbl and PEDOT:PSS incorporation preserved the hydrogel's fundamental characteristics.

The pathological consequences of PNI involve excessive ROS generation, leading to oxidative stress, protein denaturation, cellular necrosis, and persistent inflammation [30]. TA, a plant-derived polyphenol with potent antioxidant properties, effectively scavenges free radicals and mitigates intracellular ROS levels [31]. The antioxidant efficacy of the hydrogel was assessed using DPPH• and PTIO• radical scavenging assays. As illustrated in Fig. 3I and L, upon introducing the hydrogel into DPPH• and PTIO• solutions at corresponding TA concentrations, it reacted with the radicals, inducing alterations in the solution's chemical structure and resulting in a visible color change. At a concentration of 20 mg/mL, the CHs/MeCbl hydrogel demonstrated scavenging rates of 91.15 ± 0.29 % for DPPH• and 92.94 ± 0.16 % for PTIO• (Fig. 3J and M). In comparison, at the same concentrations, TA exhibited scavenging rates of 77.26 ± 0.71 % for DPPH• and 73.2 ± 0.62 % for PTIO• (Fig. 3K and N). These results demonstrate the enhanced antioxidant capacity of the hydrogel system, suggesting its potential to mitigate oxidative stress and promote PNR.

3.3. The impact of hydrogels and ES on cellular behavior

To evaluate cellular viability and proliferation, we performed live/dead staining assays on SCs and HUVECs using Calcein AM and PI as viability markers. All experimental groups maintained high cell viability without significant necrotic cell populations (Fig. 4). This indicates that neither ES nor the conductive-coated, drug-loaded hydrogel adversely
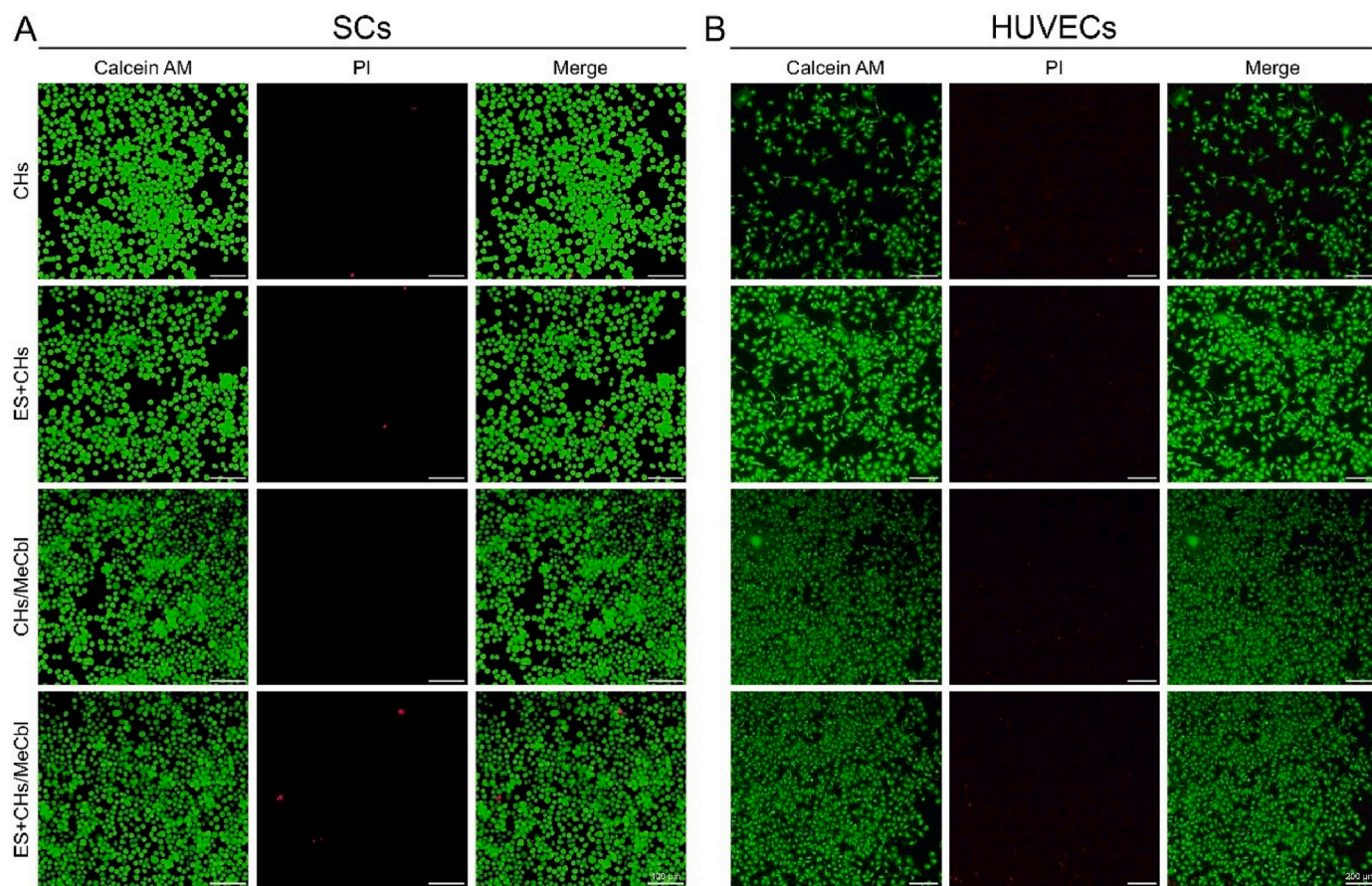
Fig. 4. The results of double staining for live/dead cells in the hydrogel extract and ES. (**A**) Representative images of double staining of SCs (the left column is calcein AM staining, the middle column is PI staining, and the right column is merged photos) (n = 3, n indicates the number of experimental replicates). (**B**) Representative images of double staining of HUVECs (the left column is calcein AM staining, the middle column is PI staining, and the right column is merged photos) (n = 3, n indicates the number of experimental replicates).

impacted cell growth. Notably, the cell density in the ES + CHs/MeCbl group was marginally higher compared to other experimental groups, indicating that the combination of ES and the CHs/MeCbl hydrogel can enhance cell proliferation. This observation aligns with previous findings by Wang et al. [32]. In summary, the CHs/MeCbl hydrogel demonstrated excellent biocompatibility, exhibiting no cytotoxicity. Furthermore, when combined with ES, it significantly promoted cell proliferation, thereby reinforcing the potential application value of this hydrogel-ES combination in the PNR.

ES has been extensively utilized in neuroscience to facilitate the nerve cell growth and proliferation [33,34]. The primary mechanism involves modulating cell membrane potential, which activates intracellular signaling pathways such as the p38 mitogen-activated protein kinase (MAPK) pathway. This pathway is crucial for the synthesis of nerve growth factors (NGFs) and neuronal survival [35]. Furthermore, ES enhances the intracellular accumulation of cyclic adenosine monophosphate (cAMP), leading to increased expression of NTFs and cytoskeletal protein synthesis, thereby promoting nerve cell growth and differentiation [36]. ES also facilitates nerve cell migration and axonal growth by modulating the local electric field, providing directional cues for neurogenesis [16]. Research has shown that ES can enhance macrophage migration to injury sites, accelerating the clearance of myelin and axonal debris, which creates a conducive microenvironment for neurogenesis [37]. Additionally, ES promotes the migration and proliferation of SCs, forming bridging structures that guide axonal regeneration [38]. Consequently, the integration of ES with hydrogels holds significant promise for enhancing nerve cell growth and proliferation.

In this study, we evaluated the blood and cellular compatibility of the hydrogel. Blood compatibility is a critical parameter for assessing biomaterial safety [39]. We conducted a hemolysis test using 2 % rat blood samples and hydrogel extracts (Fig. S3A). As shown in Fig. S3B, compared to ultrapure water as the positive control, the hemolysis rate for each hydrogel group was less than 5 %. According to ISO 10993-4 standards, these results confirm the hydrogel's excellent blood compatibility [40]. After a 24-h co-incubation of the hydrogel extract with SCs, cell viability was observed to be over 85 % (Fig. S3C). These findings suggest that the tested hydrogel exhibits no cytotoxic effects and supports robust cellular viability. Therefore, the CHs/MeCbl hydrogel demonstrates superior biocompatibility and biosafety, making it a promising candidate material for PNR.

We conducted an in-depth investigation into the hydrogel's antioxidant properties at the cellular level. To quantitatively evaluate the scavenging efficiency of intracellular ROS, we utilized the DCFH-DA probe, a cell-permeable and non-fluorescent probe that becomes fluorescent upon activation by H_2O_2 within cells [41]. SCs exposed to H_2O_2 exhibited a pronounced fluorescence signal, indicating elevated levels of intracellular ROS. Untreated SCs served as the negative control, while H_2O_2-treated SCs acted as the positive control. The experimental groups comprised SCs co-incubated with H_2O_2 followed by treatment with either hydrogel or TA. Fluorescence staining results demonstrated that the positive control group exhibited the highest fluorescence intensity. Conversely, cells treated with the hydrogel extract or TA showed a substantial decrease in fluorescence intensity, suggesting that both the hydrogel and TA effectively mitigated intracellular ROS expression under oxidative stress conditions, thereby exhibiting superior antioxidant properties (Fig. S4A). Quantitative analysis of fluorescence intensity further corroborated these findings: the positive control group had an intensity of 57.98 ± 1.08, while the hydrogel and TA groups recorded intensities of 37.2 ± 1.49 and 31 ± 0.91, respectively, both significantly lower than the positive control. These results confirm the hydrogel's efficacy in scavenging intracellular ROS, thus protecting cells from ROS-induced damage (Fig. S4B).

MeCbl, a bioactive analog of vitamin B12, has demonstrated significant antioxidant properties by effectively reducing ROS levels within biological systems [42]. The mechanism underlying its antioxidant effects primarily involves the activation of the nuclear factor erythroid 2-related factor 2 (Nrf2)/heme oxygenase-1 (HO-1) signaling pathway, thereby enhancing the activity of intracellular antioxidant enzymes and mitigating cellular damage caused by oxidative stress [43]. In biomedicine, MeCbl's antioxidant properties render it a potentially valuable agent for antioxidant therapy. Studies have demonstrated that TA, renowned for its ability to bind with polyphenolic compounds, can significantly enhance antioxidant efficacy [44]. By incorporating MeCbl and TA into hydrogel systems, a synergistic effect is observed that significantly enhances the hydrogel's antioxidant properties and more effectively mitigates ROS levels. This synergism presumably stems from the complementary mechanisms of both compounds in neutralizing free radicals and inhibiting oxidative stress responses, thereby providing superior antioxidant protection in biomaterials. Future research will explore the detailed mechanisms and potential applications of this synergistic interaction.

3.4. The degradation of hydrogel in vitro

To evaluate the safety of hydrogels for therapeutic applications *in vivo*, we assessed their biodegradability and biocompatibility through subcutaneous implantation in the dorsal region of rats. The implantation sites were photographed from the time of implantation until the 21st day (Fig. S5). By the 21st day, the hydrogels had significantly decreased in size compared to their initial dimensions. Most hydrogels had integrated with the surrounding tissues, making further weight measurements impractical. No significant inflammatory responses were observed in the peri-implant tissues. Histological examination of the subcutaneous tissues within the hydrogel regions revealed no substantial inflammatory cell aggregation or infiltration. These findings indicate that the hydrogels meet the essential criteria for therapeutic applications in animal models and exhibit excellent biocompatibility.

The degradation rate of implantable materials is a critical factor for PNR. Typically, the regeneration process for a 1 cm nerve segment takes approximately 2–3 months [16]. Commercially available nerve scaffolds approved by the Food and Drug Administration (FDA), such as Neuroflex and NeuroGen, achieve complete degradation within 8–48 months, respectively [45]. When hydrogels are implanted subcutaneously in the dorsal region of rats, the mucosal layer and tissue fluid can freely interact with the hydrogels following suture closure, significantly accelerating their degradation. However, when hydrogels are administered to the site of nerve injury, they reside within the muscle interstices of the rat's leg, reducing direct exposure to tissue fluids and digestive enzymes, which consequently slows down their degradation process.

PEDOT:PSS exhibits remarkable electrical conductivity and chemical stability. PEDOT:PSS exhibits exceptional chemical stability in both ambient and elevated-temperature aqueous environments, attributed to the stabilizing influence of sulfur and oxygen atoms on positive charges [16]. However, the limited biodegradability of CPs poses a significant challenge in the development of tissue engineering materials [46]. Strategies to address this issue include incorporation hydrolyzable side groups into monomers and synthesizing hybrid CPs with biodegradable components [47,48]. In this studies, we developed a composite material consisting of HPTA, MeCbl, and PEDOT:PSS, which was diluted to mitigate cytotoxicity while maintaining electrical conductivity. Animal experiments and H&E staining results demonstrated that the implantation of PEDOT:PSS did not significantly impair PNR.

3.5. The analysis of walking tracks and the electrophysiological analysis of the sciatic nerve

The SFI is a crucial metric for evaluating nerve functional recovery, ranging from −100 to 0, where −100 indicates complete impairment and 0 signifies full restoration of lower limb function [49]. As shown in Fig. 5A, the footprints and plantar pressure distribution of rats were
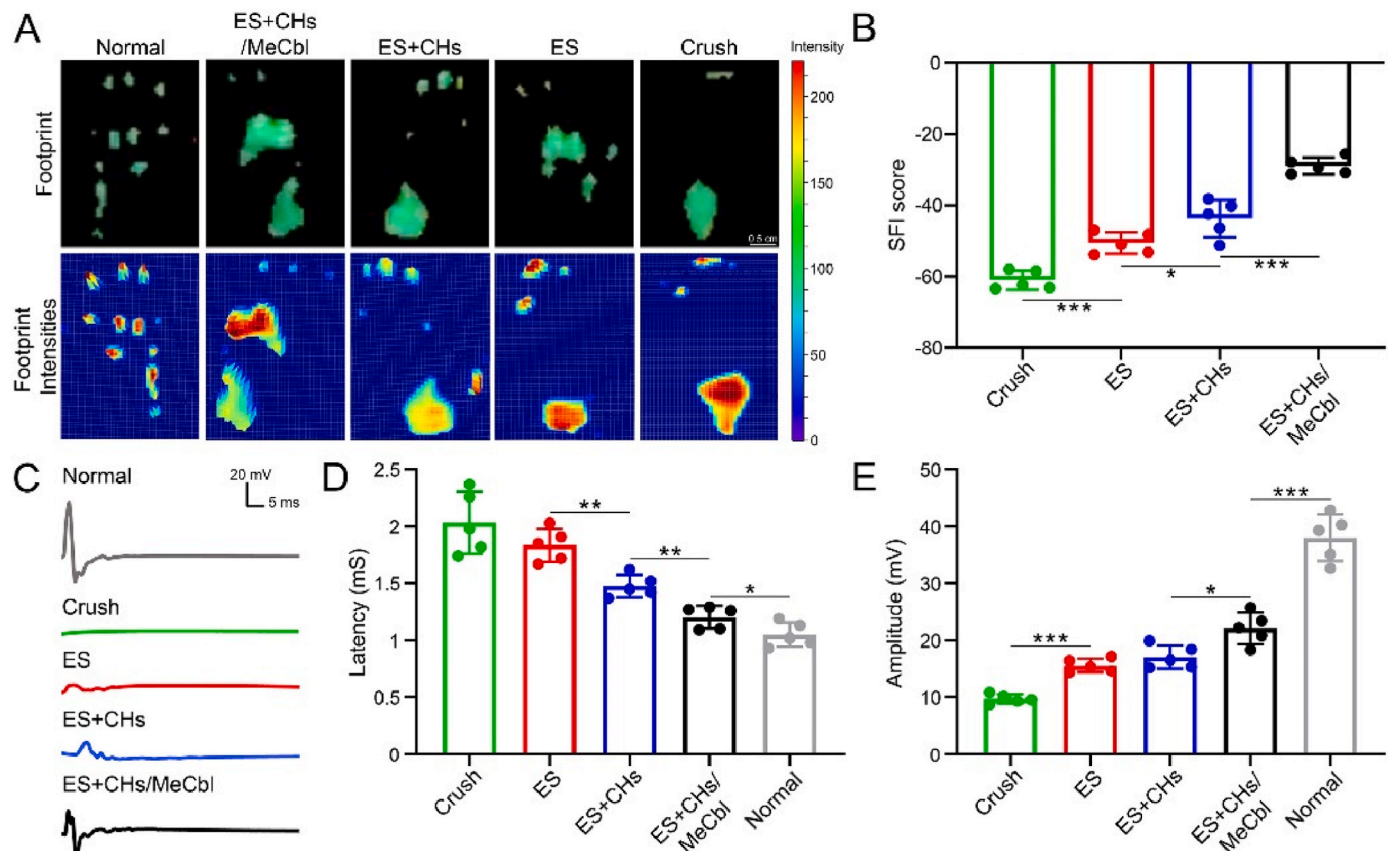
Fig. 5. The recovery of motor function and electrophysiology in the lower extremities of rats. (**A**) The rat footprints and plantar pressure intensities in each experimental group. (**B**) The SFI of rats in each experimental group (n = 5, n indicates the number of experimental animals in each group). The neurophysiological analysis includes the waveform (**C**), latency (**D**), and amplitude (**E**) of CMAPs for each group (n = 5, n indicates the number of experimental animals in each group). All statistical data are represented as mean $\pm$ SD (* indicates P < 0.05, ** indicates P < 0.01, *** indicates P < 0.001).

analyzed at the 4-week post-surgical time point. The results revealed that the interdigital distance in both the Crush and ES groups was indistinct, with significant flexion contractures and limited toe extension and abduction functions. In contrast, the footprints of the ES + CHs/MeCbl group exhibited markedly greater clarity compared to the other groups. These findings suggest that lower limb function in the Crush and ES groups had not fully recovered by the 4-week postoperative mark. Further analysis of the SFI data demonstrated that the recovery of lower limb nerve function in the ES + CHs/MeCbl group was significantly superior to that in other groups (p < 0.001). The inclusion of ES and CHs each contributed to a notable improvement in lower limb nerve function (Fig. 5B). These results indicate that ES, CHs, and MeCbl independently promote the recovery of lower limb nerve function in rats, with a synergistic effect observed among these factors.

Electrophysiological analysis is a critical method for evaluating PNR, with the amplitude and latency of CMAP serving as key parameters (Fig. 5C). CMAP was elicited through ES of the proximal nerve segment and recorded by electrodes positioned on the distal muscle. While waveforms were detected in all experimental groups, the Crush group displayed a nearly flat horizontal line, indicative of substantial impairment in nerve function. Fig. 5D illustrates the CMAP latency in rats across different experimental groups. At 4 weeks post-treatment, a comparative analysis of latencies revealed that the administration of CHs and MeCbl markedly accelerated the recovery of nerve latency, although it still lagged behind the normal nerve function. The restoration of CMAP latency following sciatic nerve injury in rats primarily indicates gradual improvements in sensory and motor functions, characterized by increased nerve conduction velocity and activation of the nerve regeneration process, including axonal and myelin regeneration.

This functional recovery is crucial for overall nerve performance and behavioral capabilities in rats [50].

The recovery of CMAP amplitude primarily reflects the enhancement of nerve conduction function, encompassing axonal and myelin regeneration, which improves the efficiency of nerve impulse conduction. This improvement also suggests enhanced responsiveness of muscles to nerve stimulation, thereby facilitating muscle function recovery [51]. Although a discrepancy in CMAP amplitude was observed between the treated rats' sciatic nerves at 4 weeks post-treatment and the control group, the ES + CHs/MeCbl group demonstrated superior amplitude recovery compared to the ES + CHs group. This finding suggests that the combination of ES with CHs/MeCbl effectively promote the recovery of both nerve conduction and lower limb muscle function (Fig. 5E).

3.6. Histological examination of sciatic nerve

To evaluate nerve tissue regeneration in each experimental group, histological analyses were performed using H&E staining, TB staining, and TEM on regenerated nerves at 4 weeks post-treatment (Fig. 6A). The H&E staining results revealed that normal nerve tissue exhibited a well-organized structure. In comparison, while the regenerated nerves in the ES + CHs/MeCbl group did not achieve the same level of organization as normal nerves, they were significantly more structured than those in other experimental groups. In contrast, the Crush group displayed loosely structured and misaligned nerve tissue, with a notable increase in vacuoles within the nerve tissue after 4 weeks of treatment. Additionally, the local inflammatory response, a critical indicator for evaluating the efficacy of PNR, showed no significant infiltration of inflammatory cells, cellular edema, or fatty degeneration in any of the
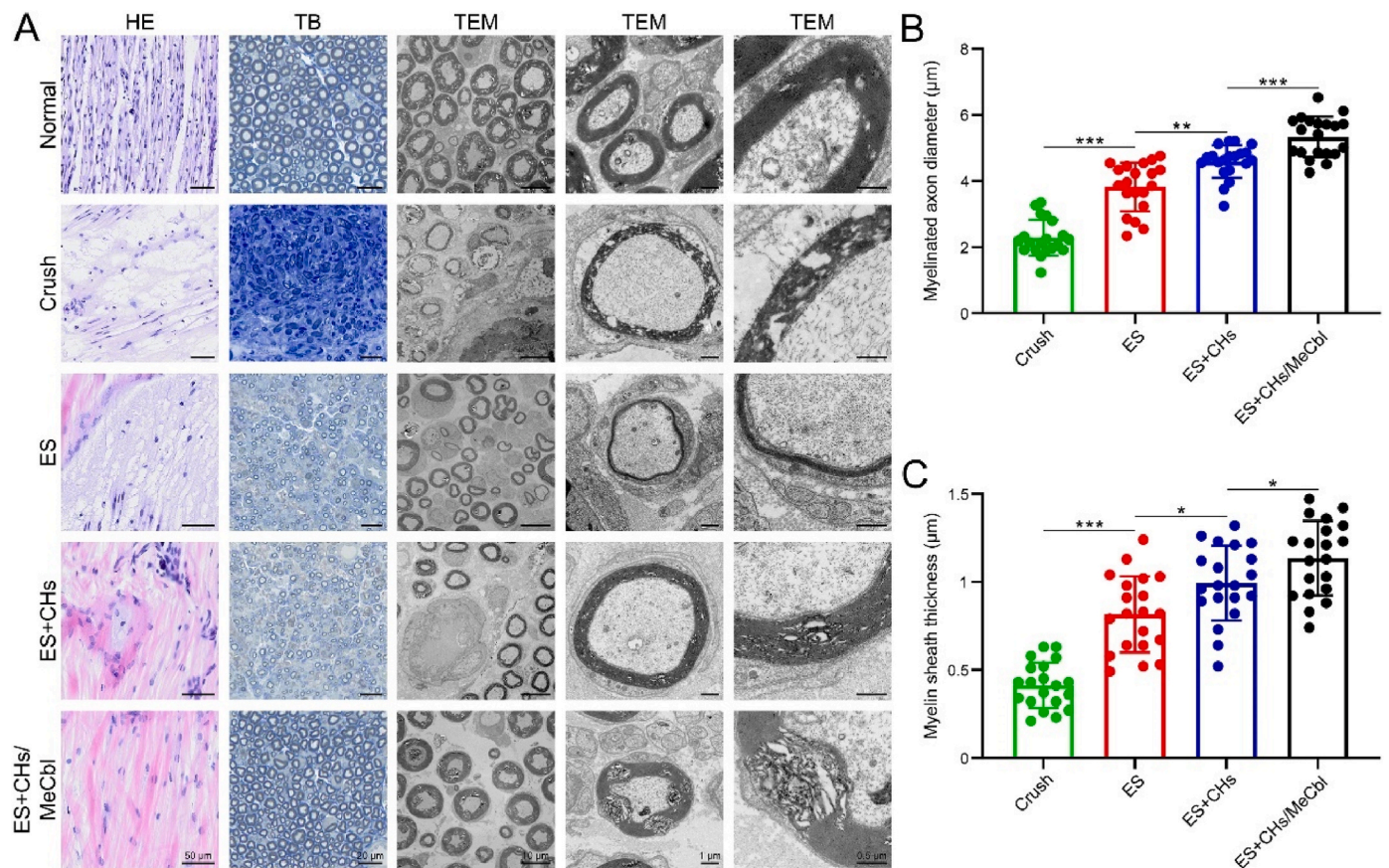
Fig. 6. Histologic examination of regenerated nerves at the 4-week post-treatment time point. (**A**) The regenerated nerves in each group evaluated using H&E staining, TB staining, and TEM images (n = 5, n indicates the number of samples tested in each group). (**B**) The diameter of myelinated axons (n = 20, n indicates the number of myelinated axons in each group) and (**C**) the thickness of the myelin sheath (n = 20, n indicates the number of myelin sheaths in each group) in each group at 4 weeks post-treatment. All statistical data are represented as mean ± SD (* indicates $P < 0.05$, ** indicates $P < 0.01$, *** indicates $P < 0.001$).

groups. These findings suggest that the treatments did not induce substantial local inflammatory reactions.

The maintenance of nerve function is intricately linked to both the quantity of myelinated axons and the extent of myelination. The number of myelinated axons directly influences nerve conduction velocity, as myelin sheaths enable saltatory conduction of nerve impulses, thereby enhancing the efficiency of signal transmission [52]. The degree of axonal myelination determines the propagation speed of action potentials, which subsequently impacts the response time and coordination within the nerve system. Furthermore, myelin serves a protective role for axons, ensuring the stability and precision of nerve signal transmission. The thickness and integrity of myelin are directly correlated with the strength and fidelity of these signals. Damage or degradation of myelin can result in nerve dysfunction [52]. Consequently, the quantity of myelinated axons and the quality of myelin are critical parameters for evaluating nerve function and the efficacy of PNR.

Using TB staining and TEM imaging of nerve cross-sections, we conducted a comprehensive analysis of the number, morphology, axon diameter, and myelin thickness of myelinated nerve fibers. At 4 weeks post-treatment, the Crush group exhibited a significant reduction in the number of nerve fibers, with many axons displaying abnormal morphology characterized by flattened or oval shapes. The distribution of myelinated axons was notably sparse, and the myelin sheaths were thinner compared to other groups. With the application of interventions such as ES, CHs, and MeCbl, a significant increase in the number of myelinated nerve fibers was observed. Axonal morphology exhibited greater regularity, while both axon diameter and myelin thickness demonstrated an upward trend. High-magnification TEM images were used to accurately measure the diameters of myelinated axons and the

thicknesses of myelin sheaths across all groups (Fig. 6B and C). The results indicated that these treatment factors facilitated the regeneration of myelinated nerve axons, demonstrating synergistic effects. The physical and chemical signals at the material interface play a pivotal role in mediating interactions between cells and CPs, while ES can modulate cell behavior by altering membrane properties [53]. However, the precise mechanisms by which cells perceive electrical signals warrant further investigation to achieve a more comprehensive understanding.

3.7. Immunofluorescence analysis of sciatic nerve

In the immunofluorescence analysis of rat sciatic nerves, we examined the expression profiles of various nerve proteins during PNR. Specifically, we focused on GFAP, an intermediate filament protein expressed in both CNS and PNS. Within the CNS, GFAP is predominantly localized in astrocytes, where it plays a critical role in maintaining cytoskeletal integrity and cellular resilience. Following PNI, the elevation in GFAP levels promote axonal regeneration by facilitating growth along the topographical cues provided by fibrous scar tissue [54]. NF200, a key neurofilament protein, serves as an indicator for evaluating the regeneration of neurofilaments during PNR. Together, neurofilaments, microfilaments, and microtubules form the neuronal cytoskeleton, which provides essential structural support for axons and regulates their diameters [55].

In addition to GFAP and NF200, we conducted immunofluorescence staining for S100 and MBP. S100 predominantly labels SCs and reactive astrocytes, whereas MBP specifically marks myeline. As the principal component of myelin in the PNS, MBP is localized on the myeline sheath membrane and plays a critical role in maintaining the structural and

functional integrity of myeline [56]. Through immunofluorescence staining of these nerve proteins, we systematically characterized the recovery of rat sciatic nerves (Fig. 7A and B). A semi-quantitative analysis of fluorescence intensity was conducted to evaluate the expression levels of specific proteins associated with PNS. The results demonstrated that the combination of ES, CHs, and MeCbl exhibited a more pronounced promoting effect on axonal regeneration and myelin formation compared to other treatment methods (Fig. 7C).

3.8. Histological examination of GM and EDL

Following PNI, muscles innervated by the injured nerve experience a loss of neurotrophic support, leading to an imbalance in muscle protein homeostasis that promotes protein degradation. This condition can result in reduced muscle cell volume, decreased muscle mass, and increased proliferation of connective tissue [57]. Compared to the contralateral healthy side, significant atrophy was observed in both GM and EDL across all experimental groups (Fig. 8A). Notably, the experimental group treated with ES + CHs/MeCbl exhibited muscle morphology that more closely resembled the healthy control, demonstrating significantly reduced muscle atrophy. Further examination using Masson's trichrome staining revealed that muscle fibers with better recovery exhibited enlarged muscle cell size and reduced perimysial fibrous connective tissue. In contrast, muscle fibers with less effective recovery displayed atrophy and increased collagen fiber proliferation. These findings suggest that effective PNR strategies can mitigate muscle atrophy and enhance the restoration of muscle structure and function.

In this study, we observed a significant reduction in the muscle weight ratio of GM on the experimental side compared to the contralateral side. The combined treatment of ES + CHs/MeCbl demonstrated notable therapeutic efficacy in attenuating muscle atrophy, while other experimental groups showed limited effectiveness (Fig. 8B). Quantitative analysis revealed that after 4 weeks treatment, all experimental groups exhibited varying degrees of GM fiber diameter restoration (Fig. 8C). While ES, CHs, and MeCbl individually contributed to lower limb muscle recovery, their combined application demonstrated synergistic therapeutic effects. Similar recovery patterns were observed in EDL, as evidenced by both weight ratio and fiber diameter measurements (Fig. 8D and E).

The functional recovery of lower limb muscles is critically dependent on sciatic nerve regeneration. This regenerative process primarily occurs through the augmentation of neuromuscular junction (NMJ) function, a vital interface for the transmission of nerve signals to muscle tissue. The release of acetylcholine (ACh) and subsequent receptor activation are pivotal in this mechanism. With the restoration of sciatic nerve function, the cross-sectional area and strength of muscle fibers also increase, highlighting the intimate relationship between PNR and muscle function recovery. Consequently, successful regeneration of the sciatic nerve not only facilitates the restoration of nerve function but also offers essential support for the functional recovery of its target organs.

The NMJ represents a specialized peripheral synapse between lower motor neurons and skeletal muscle fibers, whose structure and function have been extensively characterized across multiple species [58–60]. During embryonic development, the precise formation of NMJs is critical for establishing efficient motor signal transmission and subsequent
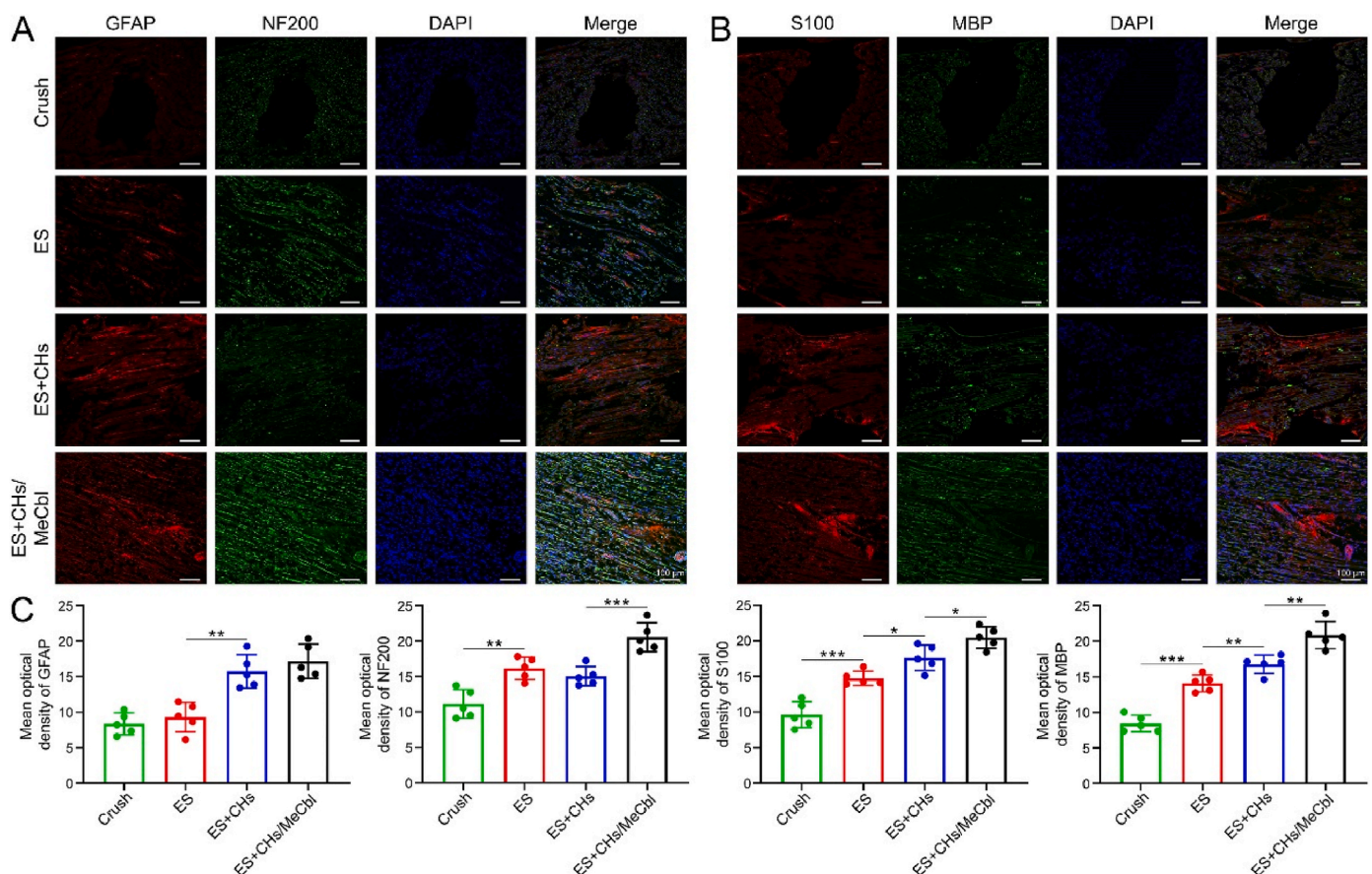
Fig. 7. Immunofluorescence analysis of sciatic nerves 4 weeks post-treatment. (A) The triple immunofluorescent staining of GFAP and NF200 (red, GFAP; green, NF200). (B) The triple immunofluorescent staining of S100 and MBP (red, S100; green, MBP). (C) Quantification of fluorescence intensity for GFAP, NF200, S100, and MBP using a semiquantitative approach (n = 5, n indicates the number of samples tested in each group). All statistical data are represented as mean ± SD (* indicates P < 0.05, ** indicates P < 0.01, *** indicates P < 0.001).
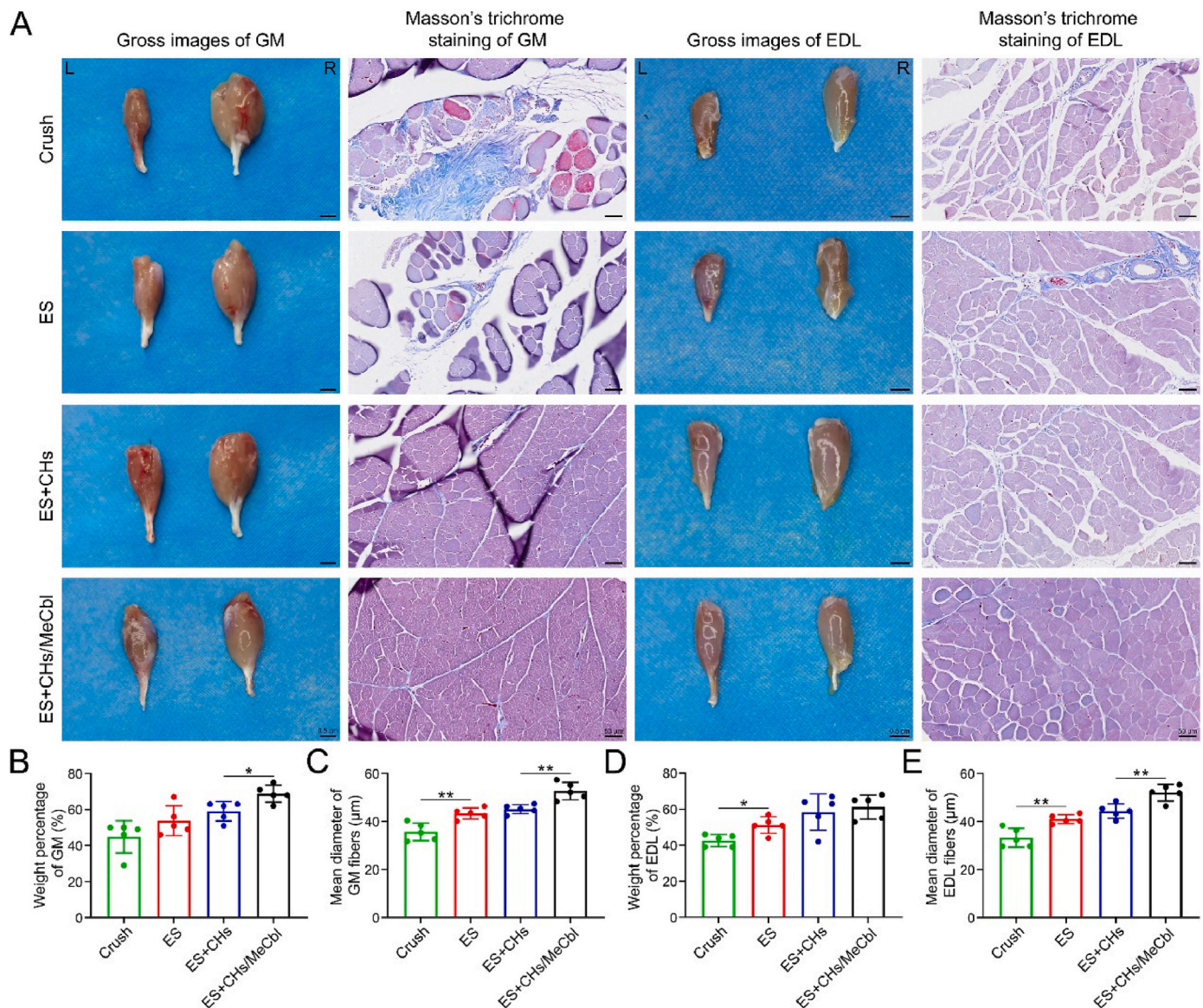
Fig. 8. Analysis of GM and EDL 4 weeks post-treatment. (**A**) Photographs of GM and EDL from each experimental group and Masson's trichrome staining of GM and EDL. (**B**) The weight ratio of GM on the experimental side to the contralateral normal side (n = 5, n indicates the number of experimental animals in each group). (**C**) The mean fiber diameter of GM on the experimental side (n = 5, n indicates the number of muscle fibers in each group). (**D**) The weight ratio of EDL on the experimental side relative to the contralateral normal side (n = 5, n indicates the number of experimental animals in each group). (**E**) The mean fiber diameter of EDL on the experimental side (n = 5, n indicates the number of muscle fibers in each group). All statistical data are represented as mean ± SD (* indicates $P < 0.05$, ** indicates $P < 0.01$).

muscle contraction [61].

In mammalian systems, NMJs undergo significant postnatal maturation, transitioning from poly-neuronal innervation at birth to mono-neuronal innervation through synaptic elimination [62]. This developmental process optimizes neural architecture and enhances signal transmission efficiency between neurons, muscles, and glial cells [63]. Concurrently, the postsynaptic membrane undergoes substantial morphological and molecular remodeling, including the formation of synaptic folds and the replacement of fetal γ-acetylcholine receptor (γ-AChR) subunit with adult ε-subunit [64,65]. Following nerve injury, NMJ degeneration often precedes axonal loss and represents a hallmark of both injury response and aging processes [61]. A key indicator of muscle denervation is the diminished intensity of endplate staining, typically resulting from AChR dispersion in the absence of neural input. Therefore, precise imaging and quantification of NMJ morphology are essential for evaluating the recovery of nerve innervation capabilities.

To accurately assess NMJ recovery, we employed a dual-staining approach combining α-BTX with NF-L and Syn antibodies. This methodology enabled precise visualization of AChRs clusters through α-BTX binding, while simultaneously mapping nerve terminal distribution and synaptic architecture via NF-L and Syn immunostaining. After 4 weeks of treatment, the ES + CHs/MeCbl group demonstrated superior recovery of MEP of GM compared to other experimental groups, accompanied by significant regeneration of nerve fibers and presynaptic membranes (Fig. 9A). The therapeutic effects of ES can be attributed to multiple mechanisms: it promotes neuronal growth and differentiation by enhancing the expression of NTFs such as brain-derived neurotrophic factor (BDNF) and NGF, while MeCbl facilitates muscle and NMJ regeneration through enhanced phosphatidylcholine synthesis and ACh metabolism. Notably, MeCbl has been shown to elevate acetylcholinesterase (AChE) activity and promote mature AChRs clustering at MEPs, thereby supporting structural and functional recovery following PNI.
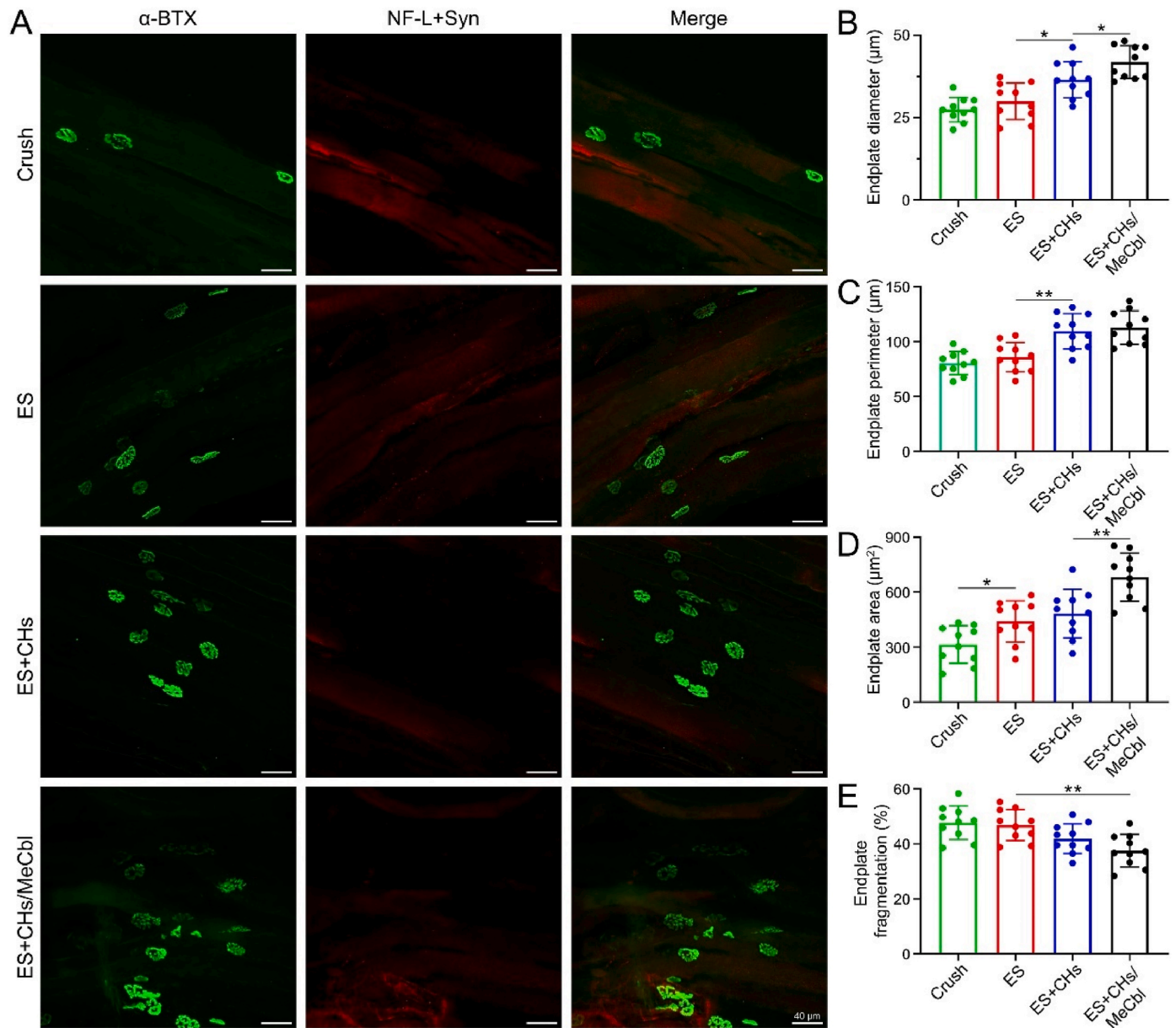
Fig. 9. Immunohistochemical staining and quantitative analysis of NMJs in GM fibers. (**A**) Rat GM fibers showing the morphology of presynaptic (NF-L + Syn, red) and postsynaptic (α-BTX, green) components of NMJs. (**B–E**) Quantitative analysis of postsynaptic MEP morphology including diameter, perimeter, area, and fragmentation rate (n = 10, where n represents the number of samples analyzed per group). All statistical data are presented as mean ± SD (*P < 0.05, **P < 0.01).

The combined treatment of ES and CHs/MeCbl significantly enhanced the morphological recovery of NMJs in the GM and markedly reduced its fragmentation rate at 4 weeks post-PNI (Fig. 9B–E). A comparable trend was observed in the NMJ characterization of the EDL (Fig. S6). Notably, no significant differences in NMJ morphology were found between the GM and EDL, consistent with previous studies [64]. Research has demonstrated a significant correlation between muscle fiber type and NMJ diameter, with smaller NMJ diameters more frequently associated with fast-twitch muscle fibers. Conversely, larger NMJ areas tend to be observed in muscles with a lower proportion of fast-twitch fibers [66,67]. However, some studies suggested that muscle fiber diameter might not be the primary determinant of synaptic structure [64]. Future investigations should aim to elucidate the precise relationship between NMJ characteristics and their associated muscle fibers.

Mammalian skeletal muscle is predominantly comprised of 2 functionally distinct types of muscle fibers: slow-twitch (type I) and fast-

twitch (type II) fibers. These fiber types exhibit notable differences in their anatomical structure, physiological characteristics, and metabolic pathways [68]. Based on the differential expression of MYH genes, fast-twitch muscle fibers can be further classified into 3 subtypes: type IIa (expressing MYH2), type IIx (expressing MYH1), and type IIb (expressing MYH4) [69]. The contraction time and fatigue resistance of fast-twitch muscle fibers are shorter than those of slow-twitch fibers, showing a decreasing trend from type IIa to type IIb. Type IIa fibers possess oxidative characteristics and most closely resemble slow-twitch muscle fibers, while type IIx and type IIb fibers exhibit glycolytic properties. Type IIb fibers are particularly crucial for short-duration, high-intensity movements. Regarding size differences among muscle fiber subtypes, research findings have been inconsistent, potentially due to variations in fiber diameters across different muscle types [70]. Nevertheless, it is generally observed that slow-twitch muscle fibers have smaller diameters compared to fast-twitch fibers, with type IIb fibers exhibiting the largest diameter [71].

In the immunofluorescence staining results for the muscle fibers of GM (Fig. 10A), the density of fast-twitch muscle fibers in the Crush and ES groups was significantly higher than that in the ES + CHs/MeCbl group. This increase may be attributed to the transformation of slow-twitch muscle fibers into fast-twitch muscle fibers due to atrophy [72] (Fig. 10B). Although the ES + CHs and ES + CHs/MeCbl groups showed an increased proportion of slow-twitch muscle fibers in the GM compared to other experimental groups, this proportion did not reach the previously reported range of 86–93 % [70] (Fig. 10C). Furthermore, the combined treatment of ES + CHs/MeCbl significantly increased the cross-sectional area of slow-twitch muscle fibers in the GM. In contrast, no significant changes were observed in the cross-sectional area of fast-twitch muscle fibers (Fig. 10D and E).

Immunofluorescence staining results for the muscle fibers of EDL are presented in Fig. S7A. The density of slow-twitch muscle fibers in the EDL was lower than that in the GM, consistent with the distinct motor characteristics of these muscles and in agreement with previous studies [70]. Although no significant differences were observed in the number and cross-sectional area of fast-twitch muscle fibers in the EDL across the groups, the ES + CHs/MeCbl treatment demonstrated a beneficial effect on the recovery of both the number and cross-sectional area of slow-twitch muscle fibers (Figs. S7B–E).

Muscle atrophy differentially affects various muscle fiber types, often leading to specific alterations in fiber characteristics. Typically, atrophy predominantly impacts either type I or type II fibers, resulting in a shift from slow-twitch to fast-twitch muscle fiber or vice versa. Denervation primarily induces a transformation of muscle fiber types and MYH isoforms from slow-twitch to fast-twitch fiber [73]. However, the response of the same fiber type to denervation can vary depending on the specific muscle involved. For example, in rats, slow type I fibers of the soleus muscle exhibit significant atrophy following denervation. In contrast, fast type I fibers of the EDL maintain a relatively stable size during the initial 2 weeks after sciatic nerve transection. The GM, which comprises a mixture of muscle fiber types, undergoes atrophy of its slow muscle fibers and their subsequent conversion to fast muscle fibers following

PNI [72].

The treatment of ES + CHs/MeCbl significantly increased both the diameter and number of slow-twitch muscle fibers in the GM, suggesting that this combined treatment may promote a phenotypic shift from fast-twitch to slow-twitch muscle fiber types. This study provides strong scientific evidence supporting the use of ES + CHs/MeCbl for promoting PNR and subsequently restoring target organ function.

We administered 100 µL of hydrogel into the GM and EDL of rats and evaluated the biocompatibility of the hydrogel by assessing the positive expression of CD11b and CD68 through immunohistochemical staining on the 14th day post-injection. CD11b is a broadly expressed molecular marker on the surface of neutrophils and monocytes/macrophages, while CD68 serves as a specific marker for macrophages [74]. Immunofluorescence imaging revealed minimal aggregation of inflammatory cells within muscle tissues (Figs. S8 and S9). Furthermore, quantitative analysis of the immunofluorescence data confirmed the absence of significant differences among the groups (Figs. S10 and S11). These results indicate that the injected hydrogel did not induce notable inflammatory responses, demonstrating its excellent biocompatibility.

3.9. Transcriptomic analysis of sciatic nerve

We summarized the results of transcriptomic testing on animal specimens, with a focus on data quality. RNA integrity was assessed using the RNA nano 6000 assay kit of the Bioanalyzer 2100 system (Agilent Technologies, CA, USA). After raw data filtering, the sequencing error rate and GC content distribution were evaluated to obtain clean reads and data for subsequent analysis. These findings are presented in Table 2. To avoid false-negative results, the number of raw bases was required to exceed 6G, and all our samples met the criteria. For all samples, the percentage of bases in the Q20 index (error rate <1 %) exceeded 96 %, while the percentage of bases in the Q30 index (error rate <0.1 %) was above 92 %, confirming the validity of our sequencing data.

The transcriptomics results were statistically analyzed to identify
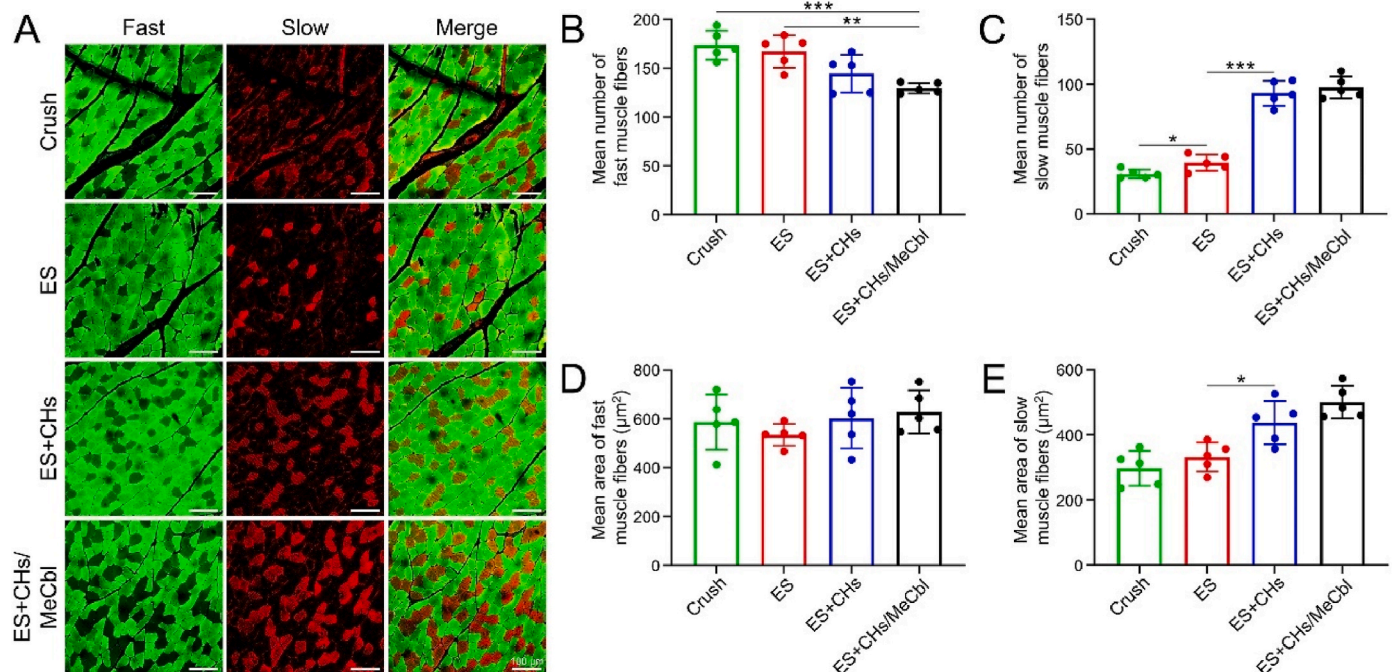
Fig. 10. Immunofluorescence staining analysis of fast and slow muscle fibers in the GM. (**A**) Immunofluorescence staining of fast muscle fibers (green) and slow muscle fibers (red). (**B**) The mean number of fast muscle fibers per unit area in the cross-section of the GM. (**C**) The mean number of slow muscle fibers per unit area in the cross-section of the GM. (**D**) The mean cross-sectional area of fast muscle fibers in the GM. (**E**) The mean cross-sectional area of slow muscle fibers in the GM. (n = 5, n indicates the number of samples tested in each group). All statistical data are represented as mean ± SD (* indicates P < 0.05, ** indicates P < 0.01, *** indicates P < 0.001).

Table 2
Summary of sample sequencing data quality.

Sample	Raw-bases	Clean-reads	Clean-bases	Error-rate	Q20	Q30	GC-pct
Crush-1	7.09G	45450938	6.82G	0.01	97.71	93.57	50.26
Crush-2	7.58G	48321416	7.25G	0.01	97.87	93.95	48.52
Crush-3	7.59G	48002716	7.2G	0.01	98.16	94.75	49.49
ES-1	7.15G	45011774	6.75G	0.01	98.24	94.97	49.67
ES-2	6.94G	44040954	6.61G	0.01	98.19	94.83	50.44
ES-3	7.3G	45164928	6.77G	0.01	97.45	92.9	49.92
ES + CHs/MeCbl-1	7.57G	47441548	7.12G	0.01	97.51	93.14	49.7
ES + CHs/MeCbl −2	7.05G	44122932	6.62G	0.01	97.56	93.27	50.36
ES + CHs/MeCbl −3	8.55G	54361316	8.15G	0.01	97.43	92.88	50.1

DEGs. As shown in the volcano plot, 162 upregulated and 202 down-regulated DEGs were identified between the ES group and the Crush group. The higher number of DEGs between these groups suggests significant disparities in the processes and mechanisms involved in rat sciatic nerve regeneration. Enrichment analysis revealed that the DEGs were predominantly enriched in biological processes, including the regulation of purine nucleotide metabolism, nucleotide biosynthesis, and erythrocyte homeostasis. Notably, in the context of endogenous stem cell-mediated regeneration following PNI, key signaling pathways such as the transmembrane receptor protein tyrosine kinase signaling pathway and the MAPK signaling cascade were prominently involved. These pathways play crucial roles in cellular signal reception and transduction, thereby regulating gene expression at the cellular level (Fig. 11A) [75].

Volcano plot analysis revealed that, compared to the ES group, the ES + CHs/MeCbl group exhibited 2065 significantly upregulated and 2261 significantly downregulated DEGs. GO and KEGG pathway analyses indicated that CHs and MeCbl primarily facilitate nerve function recovery by modulating pathways associated with precursor metabolite synthesis, energy production, cellular respiration, oxidative phosphorylation, amino acid degradation, and carbon metabolism. These biological processes are essential for cellular signal reception and transduction (Fig. 11B). Furthermore, a comparative analysis between the ES + CHs/MeCbl group and the Crush group identified 1952 upregulated and 1596 downregulated DEGs. GO and KEGG pathway analyses demonstrated that the combined treatment of ES + CHs/MeCbl integrates the effects of ES and CHs/MeCbl, influencing critical biological processes such as monovalent inorganic cation transmembrane transport, proton transmembrane transporter activity, oxidoreductase activity, amino acid metabolism, carbohydrate metabolism, and carbon metabolism (Fig. 11C). The synergistic effects of ES, CHs, and MeCbl significantly enhanced the recovery of hindlimb function in rats, making the ES + CHs/MeCbl group the most effective treatment for PNR among all experimental groups in this study.

3.10. The evaluation of nutritional status and organ toxicity in rats

Histopathological examination of the heart, liver, spleen, lungs, and kidneys of rats revealed no significant abnormalities in tissue morphology or structure during the nerve regeneration period (Fig. S12). These findings suggest that neither the ES treatment nor the degradation process of the hydrogel induced inflammatory responses or exhibited toxic effects on the rats. After the treatment period, no statistically significant differences in weight changes were observed among the groups (Fig. S13), indicating that the experimental animals maintained good nutritional status, were housed under appropriate breeding conditions, and had sufficient access to food and water, with effective control of inter-cage interference. Despite lower limb dysfunction, this impairment did not hinder the animals' ability to access water and food, resulting in a trend of weight gain. The frequent administration of anesthesia and ES in the early stages of treatment may have slightly influenced the growth status of the rats. However, weight monitoring during the first 10 days post-surgery indicated minimal physiological effects, with continuous weight gain observed. The consistent increase in body weight further suggests that the PNR process occurred under favorable physiological conditions.

4. Innovation, application, and efficacy of the multifunctional hydrogel for PNR

This study presents a novel multifunctional hydrogel system that integrates MeCbl, PEDOT:PSS, and HA to synergistically enhance PNR. Unlike conventional approaches that rely on single-function materials, our hydrogel combines the benefits of sustained drug release, electrical conductivity, and microenvironment modulation, offering a comprehensive solution for PNR. The incorporation of MeCbl provides neurotrophic support, while PEDOT:PSS mimics the electrophysiological properties of native nerve tissue, and HA creates a biocompatible and hydrating microenvironment. Furthermore, the application of external ES enhances the therapeutic efficacy by promoting axonal growth and functional recovery. This multifunctional design represents a significant advancement over existing PNR strategies, which often fail to address the complex requirements of PNR.

The practical application value of this hydrogel lies in its potential to address critical challenges in clinical PNR. For instance, its injectable nature allows for minimally invasive delivery, reducing the need for complex surgical procedures. The hydrogel's tunable mechanical properties and biodegradability ensure compatibility with the dynamic PNR process, while its ability to sustain the release of MeCbl and deliver ES provides a continuous therapeutic effect. These features make it particularly suitable for treating traumatic nerve injuries, postoperative nerve dysfunction, and even chronic nerve damage. Moreover, the hydrogel's excellent biocompatibility and low immunogenicity minimize the risk of adverse reactions, further supporting its potential for clinical translation.

Our experimental results demonstrate the significant advantages of this hydrogel in promoting PNR. The combination of MeCbl and PEDOT:PSS not only enhanced axonal growth but also improved electrophysiological recovery, as evidenced by the increased amplitude and reduced latency of CMAPs. The application of ES further amplified these effects, highlighting the importance of integrating multiple therapeutic modalities. Additionally, the hydrogel's ability to modulate the local microenvironment contributed to reduced secondary damage and improved functional outcomes. These findings underscore the potential of our hydrogel to outperform traditional PNR methods, which often fail to achieve comprehensive functional recovery.

5. The limitations of the current research and directions for future studies

In this study, the concurrent application of ES, CHs, and MeCbl has demonstrated promising therapeutic effects. However, further research is necessary to optimize stimulation parameters, synchronize the degradation rate of CHs with the pace of PNR, and ascertain the most effective release mode for MeCbl. Moreover, the long-term efficacy and potential adverse effects of these interventions necessitate validation
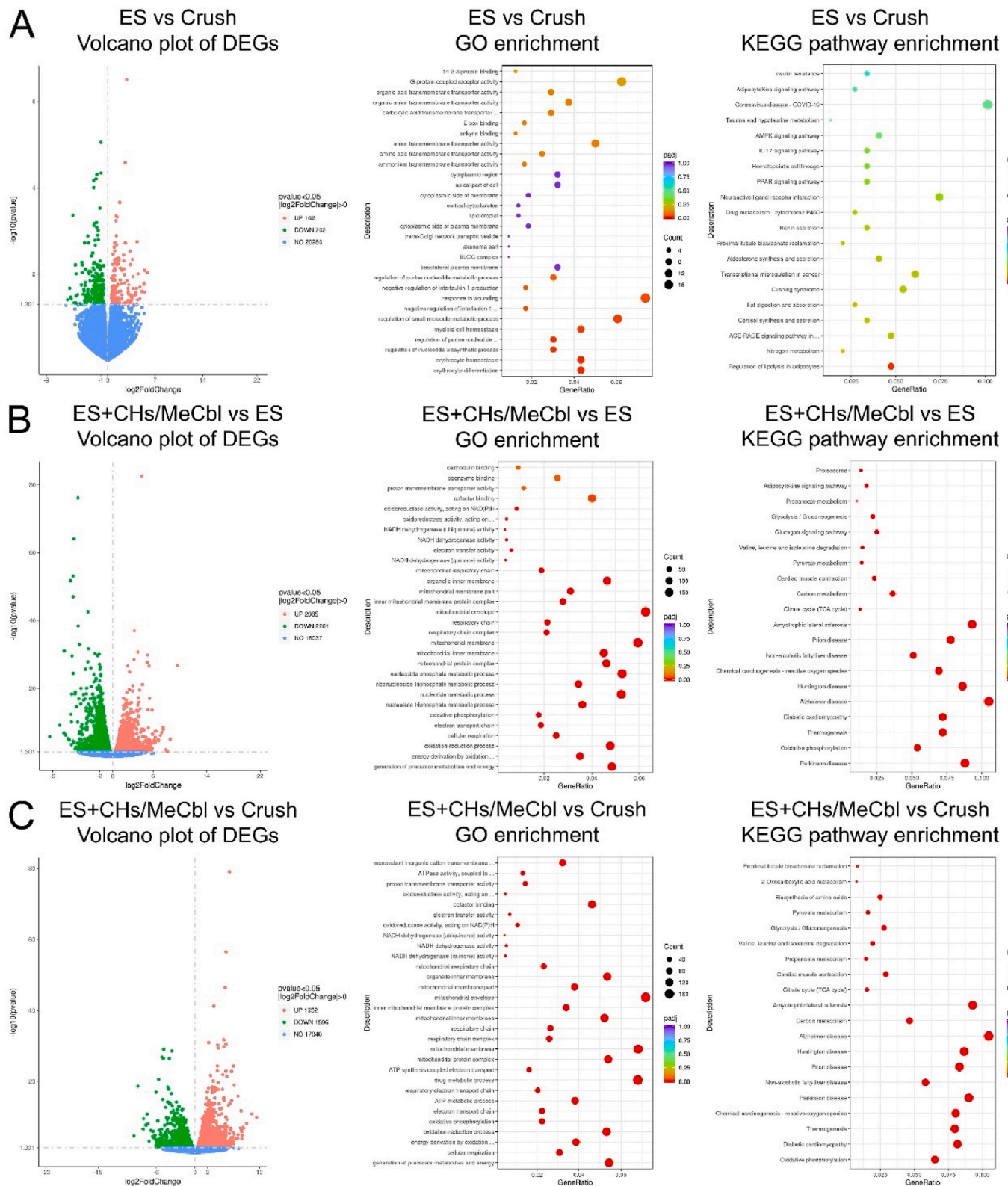
Fig. 11. Transcriptomic profiles of sciatic nerves. (**A**) The volcano plot illustrating the DEGs between the ES group and the Crush group. The significantly upregulated DEGs are represented by red dots, while the downregulated DEGs are indicated by green dots. GO enrichment analyses and KEGG pathway enrichment analyses were performed to compare functional differences in both groups (n = 3, n indicates the number of samples tested in each group). (**B**) The volcano plot comparing DEGs between the ES + CHs/MeCbl group and the ES group. Significantly upregulated DEGs are represented by red dots, while the downregulated DEGs are indicated by green dots. GO enrichment analyses and KEGG pathway enrichment analyses were conducted to explore the functional annotations and pathways associated with these groups (n = 3, n indicates the number of samples tested in each group). (**C**) The volcano plot comparing DEGs between the ES + CHs/MeCbl group and the Crush group. Significantly upregulated DEGs are represented by red dots, while the downregulated DEGs are indicated by green dots. GO enrichment analyses and KEGG pathway enrichment analyses were performed to identify the functional annotations and pathways associated with these groups (n = 3, n indicates the number of samples tested in each group).

through more comprehensive studies.

Future research directions should prioritize the development of personalized treatment protocols, fine-tuning of ES parameters, and exploration of the synergistic effects of CHs and MeCbl across diverse nerve injury models. Specifically, it is recommended to further optimize the formulation of hydrogels to enhance their mechanical properties, biocompatibility, and degradation profiles, ensuring better alignment with the PNR process. Additionally, investigating the application of these hydrogels in other types of nerve injuries, such as peripheral nerve crush injuries or central nervous system injuries, could broaden the therapeutic potential of this approach.

An in-depth investigation into the molecular mechanisms underlying these interventions during PNR process will provide a more robust scientific foundation for clinical applications. Future studies should also concentrate on refining multimodal treatment strategies and employing advanced high-resolution imaging techniques and molecular biology methodologies to evaluate therapeutic outcomes. Furthermore, executing multicenter clinical trials to assess the safety and efficacy of these therapies in human subjects represents a pivotal step in advancing the field. These studies will not only provide critical insights into the mechanisms by which ES, CHs, and MeCbl facilitate PNR but also offer robust scientific evidence to guide the development of novel therapeutic strategies.

6. Conclusion

In this study, we successfully developed a novel composite hydrogel, CHs/MeCbl, by incorporating MeCbl and PEDOT:PSS into the HA hydrogel. This hydrogel was subsequently used in combination with ES for the treatment of PNI in rats. The hydrogel exhibits an excellent porous internal structure, enabling efficient drug loading and release, as well as superior self-healing, injectability, adhesiveness, antioxidant, and degradation properties. Moreover, CHs/MeCbl demonstrates remarkable biocompatibility, promoting cell proliferation without inducing cytotoxicity. Results from animal experiments further confirm that the combined therapy of CHs/MeCbl and ES significantly enhances the recovery of hindlimb function in rats and optimizes the efficacy of PNR. These findings not only provide novel strategies for the treatment of PNI but also establish a strong scientific foundation for future research.

CRediT authorship contribution statement

Kai Liu: Writing – original draft, Visualization, Validation, Software, Methodology, Investigation. **Jiangbo Shao:** Validation, Software, Methodology, Investigation, Conceptualization. **Beibei Han:** Visualization, Software, Methodology, Investigation. **Jianfeng Liu:** Validation, Software, Methodology. **Shuai Yan:** Visualization, Software, Investigation. **Bin Liu:** Writing – review & editing, Supervision, Resources, Project administration, Funding acquisition. **Yao Liu:** Writing – review & editing, Visualization, Validation, Supervision, Resources, Project administration, Funding acquisition.

Funding sources

List of abbreviations

(continued)

3-APBA	3-Aminophenylboronic acid
3-APBA	3-Aminophenylboronic acid
3D	Three-dimensional
Ach	Acetylcholine
AChE	Acetylcholinesterase
γ-AChR	γ-Acetylcholine receptor
BDNF	Brain-derived neurotrophic factor
BTX	Bungarotoxin
cAMP	Cyclic adenosine monophosphate
CCK-8	Cell counting kit-8
CHs	Conductive hydrogels
CLSM	Confocal laser scanning microscope
CMAPs	Compound muscle action potentials
CNS	Central nerve system
CPs	Conductive polymers
DAPI	4′,6-diamidino-2-phenylindole
DC	Direct current
DCFH-DA	2′,7′-dichlorodihydrofluorescein diacetate
DEGs	Differentially expressed genes
DMEM	Dulbecco's modified eagle medium
DPPH•	2,2-diphenyl-1-picrylhydrazyl-hydrate
EDC	1-ethyl-3(3 dimethyl amino-propyl)-2-carbodiimide
EDL	Extensor digitorum longus
ES	Electrical stimulation
FDA	Food and Drug Administration
GFAP	Glial fibrillary acidic protein
GM	Gastrocnemius muscle
GO	Gene ontology
GSEA	Gene set enrichment analysis
HA	Hyaluronic acid
HCl	Hydrochloric acid
H&E	Hematoxylin-eosin
HO-1	Heme oxygenase-1
HUVECs	Human umbilical vein endothelial cells
IT	Intermediary toe
KEGG	Kyoto encyclopedia of genes and genomes
MAPK	Mitogen-activated protein kinase
MBP	Myelin basic protein
MeCbl	Mecobalamin
MEP	Motor endplate
MYH	Myosin heavy chain
NF200	Neurofilament-200
NF-L	Neurofilament-L
NGCs	Nerve guidance conduits
NGFs	Nerve growth factors
NHS	N-hydroxysuccinimide
NMJ	Neuromuscular junction
Nrf2	Nuclear factor erythroid 2-related factor 2
NTFs	Neurotrophic factors
OD	Optical density
PBS	Phosphate-buffered saline
PEDOT:PSS	Poly(3,4-ethylenedioxythiophene):polystyrene sulfonate
PFA	Paraformaldehyde
PI	Propidium iodide
PL	Paw length
PNI	Peripheral nerve injury
PNR	Peripheral nerve regeneration
PNS	Peripheral nerve system
PTIO•	2-Phenyl-4,4,5,5-tetramethylimidazoline-1-oxyl 3-Oxide
ROS	Reactive oxygen species
SCs	Schwann cells
SD	Sprague-Dawley
SD	Standard deviation
SEM	Scanning electron microscope
SFI	Sciatic functional index
Syn	Synaptophysin
TA	Tannic acid
TB	Toluidine blue
TCP	Tissue culture polystyrene
TEM	Transmission electron microscope
TS	Toe spread
UVS	Ultra-Violet spectrophotometer

Declaration of competing interest

The authors declare that they have no known competing financial interests or personal relationships that could have appeared to influence the work reported in this paper.

Appendix A. Supplementary data

Supplementary data to this article can be found online at https://doi.org/10.1016/j.mtbio.2025.101755.

Data availability

Data will be made available on request.

References

[1] Y. Yang, C. Rao, T. Yin, S. Wang, H. Shi, X. Yan, et al., Application and underlying mechanism of acupuncture for the nerve repair after peripheral nerve injury: remodeling of nerve system, Front. Cell. Neurosci. 17 (2023) 1253438, https://doi.org/10.3389/fncel.2023.1253438.

[2] F. Mankavi, R. Ibrahim, H. Wang, Advances in biomimetic nerve guidance conduits for peripheral nerve regeneration, Nanomaterials 13 (18) (2023), https://doi.org/10.3390/nano13182528.

[3] O. Taisescu, V.C. Dinescu, A.D. Rotaru-Zavaleanu, A. Gresita, M. Hadjiargyrou, Hydrogels for peripheral nerve repair: emerging materials and therapeutic applications, Gels (Basel, Switzerland) 11 (2) (2025), https://doi.org/10.3390/gels11020126.

[4] T. Wan, Q.C. Li, F.S. Zhang, X.M. Zhang, N. Han, P.X. Zhang, Biomimetic ECM nerve guidance conduit with dynamic 3D interconnected porous network and sustained IGF-1 delivery for enhanced peripheral nerve regeneration and immune modulation, Materials today Bio 30 (2025) 101403, https://doi.org/10.1016/j.mtbio.2024.101403.

[5] J. Park, J. Kim, G. Choe, Y. Jung, J.Y. Lee, Conductive hydrogel luminal filler for peripheral nerve regeneration, Biomaterials 317 (2025) 123103, https://doi.org/10.1016/j.biomaterials.2025.123103.

[6] J. Meng, J. Sun, J. Kang, S. Ren, M. Xu, R. Li, et al., Multifunctional hydrogels loaded with tellurium nanozyme for spinal cord injury repair, Materials today Bio 29 (2024) 101339, https://doi.org/10.1016/j.mtbio.2024.101339.

[7] Z. Gong, Z. Chen, D. Li, X. Lu, J. Wu, H. Sun, et al., Hydrogel loaded with cerium-manganese nanoparticles and nerve growth factor enhances spinal cord injury repair by modulating immune microenvironment and promoting neuronal regeneration, J. Nanobiotechnol. 23 (1) (2025) 29, https://doi.org/10.1186/s12951-025-03098-3.

[8] W. Shi, Y. Kong, Y. Su, M.A. Kuss, X. Jiang, X. Li, et al., Tannic acid-inspired, self-healing, and dual stimuli responsive dynamic hydrogel with potent antibacterial and anti-oxidative properties, J. Mater. Chem. B 9 (35) (2021) 7182–7195, https://doi.org/10.1039/d1tb00156f.

[9] I. Gülçin, Z. Huyut, M. Elmastas, H.Y. Aboul-Enein, Radical scavenging and antioxidant activity of tannic acid, Arab. J. Chem. 3 (1) (2010) 43–53, https://doi.org/10.1016/j.arabjc.2009.12.008.

[10] X. Li, B. Chen, X. Zhao, D. Chen, 2-Phenyl-4,4,5,5-tetramethylimidazoline-1-oxyl 3-oxide radical (PTIO•) trapping activity and mechanisms of 16 phenolic xanthones, Molecules 23 (7) (2018), https://doi.org/10.3390/molecules23071692.

[11] M. Rouabhia, H.J. Park, A. Abedin-Do, Y. Douville, M. Méthot, Z. Zhang, Electrical stimulation promotes the proliferation of human keratinocytes, increases the production of keratin 5 and 14, and increases the phosphorylation of ERK1/2 and p38 MAP kinases, Journal of tissue engineering and regenerative medicine 14 (7) (2020) 909–919, https://doi.org/10.1002/term.3040.

[12] J. Senanayake, R.R. Mattingly, H.G. Sundararaghavan, Electrical stimulation of Schwann cells on electrospun hyaluronic acid carbon nanotube fibers, PLoS One 19 (8) (2024) e0308207, https://doi.org/10.1371/journal.pone.0308207.

[13] Z. Zhang, Y. Lv, J. Harati, J. Song, P. Du, P. Ou, et al., Submicron-grooved films modulate the directional alignment and biological function of Schwann cells, J. Funct. Biomater. 14 (5) (2023), https://doi.org/10.3390/jfb14050238.

[14] S. Knorr, L. Rauschenberger, T. Lang, J. Volkmann, C.W. Ip, Multifactorial assessment of motor behavior in rats after unilateral sciatic nerve crush injury, J. Vis. Exp. 173 (2021), https://doi.org/10.3791/62606.

[15] J. Zhang, X. Zhang, C. Wang, F. Li, Z. Qiao, L. Zeng, et al., Conductive composite fiber with optimized alignment guides neural regeneration under electrical stimulation, Adv. Healthcare Mater. 10 (3) (2021) e2000604, https://doi.org/10.1002/adhm.202000604.

[16] K. Liu, S. Yan, Y. Liu, J. Liu, R. Li, L. Zhao, et al., Conductive and alignment-optimized porous fiber conduits with electrical stimulation for peripheral nerve regeneration, Materials today Bio 26 (2024) 101064, https://doi.org/10.1016/j.mtbio.2024.101064.

[17] M. Zhang, H. An, Z. Gu, Z. Huang, F. Zhang, B.G. Jiang, et al., Mimosa-Inspired stimuli-responsive curling bioadhesive tape promotes peripheral nerve regeneration, Advanced materials (Deerfield Beach, Fla) 35 (32) (2023) e2212015, https://doi.org/10.1002/adma.202212015.

[18] M. Pertea, G.M. Pertea, C.M. Antonescu, T.C. Chang, J.T. Mendell, S.L. Salzberg, StringTie enables improved reconstruction of a transcriptome from RNA-seq reads, Nat. Biotechnol. 33 (3) (2015) 290–295, https://doi.org/10.1038/nbt.3122.

[19] A.A. Gharia, C.J. Bradfield, E.P.W. Jenkins, I.D.C. Fraser, G.G. Malliaras, Efficient electroporation in primary cells with PEDOT:PSS electrodes, Sci. Adv. 10 (43) (2024) eado5042, https://doi.org/10.1126/sciadv.ado5042.

[20] P. Gkoupidenis, N. Schaefer, B. Garlan, G.G. Malliaras, Neuromorphic functions in PEDOT:PSS organic electrochemical transistors, Advanced materials (Deerfield Beach, Fla) 27 (44) (2015) 7176–7180, https://doi.org/10.1002/adma.201503674.

[21] A. Pisciotta, A. Lunghi, G. Bertani, R. Di Tinco, L. Bertoni, G. Orlandi, et al., PEDOT: PSS promotes neurogenic commitment of neural crest-derived stem cells, Front. Physiol. 13 (2022) 930804, https://doi.org/10.3389/fphys.2022.930804.

[22] M.H. Mahmoudinezhad, A. Karkhaneh, K. Jadidi, Effect of PEDOT:PSS in tissue engineering composite scaffold on improvement and maintenance of endothelial cell function, Journal of biosciences 43 (2) (2018) 307–319.

[23] G. Yang, D. Gou, L.K. Bu, X.Y. Wei, H. Hu, W.B. Huo, et al., Developmental toxicity of PEDOT:PSS in zebrafish: effects on morphology, cardiac function, and intestinal Health, Toxics 12 (2) (2024), https://doi.org/10.3390/toxics12020150.

[24] C. Liu, L. Fan, J. Xing, Q. Wang, C. Lin, C. Liu, et al., Inhibition of astrocytic differentiation of transplanted neural stem cells by chondroitin sulfate methacrylate hydrogels for the repair of injured spinal cord, Biomater. Sci. 7 (5) (2019) 1995–2008, https://doi.org/10.1039/c8bm01363b.

[25] R. Davis, A. Singh, M.J. Jackson, R.T. Coelho, D. Prakash, C.P. Charalambous, et al., A comprehensive review on metallic implant biomaterials and their subtractive manufacturing, The International journal, advanced manufacturing technology 120 (3–4) (2022) 1473–1530, https://doi.org/10.1007/s00170-022-08770-8.

[26] B. Hosseinzadeh, M. Ahmadi, Degradable hydrogels: design mechanisms and versatile applications, Materials Today Sustainability 23 (2023), https://doi.org/10.1016/j.mtsust.2023.100468.

[27] T. Yang, M. Yang, C. Xu, K. Yang, Y. Su, Y. Ye, et al., PEDOT:PSS hydrogels with high conductivity and biocompatibility for in situ cell sensing, J. Mater. Chem. B 11 (14) (2023) 3226–3235, https://doi.org/10.1039/d3tb00014a.

[28] D. Zhang, W. Yang, C. Wang, H. Zheng, Z. Liu, Z. Chen, et al., Methylcobalamin-loaded PLCL conduits facilitate the peripheral nerve regeneration, Macromol. Biosci. 20 (3) (2020) e1900382, https://doi.org/10.1002/mabi.201900382.

[29] S. Nishimoto, H. Tanaka, M. Okamoto, K. Okada, T. Murase, H. Yoshikawa, Methylcobalamin promotes the differentiation of Schwann cells and remyelination in lysophosphatidylcholine-induced demyelination of the rat sciatic nerve, Front. Cell. Neurosci. 9 (2015) 298, https://doi.org/10.3389/fncel.2015.00298.

[30] X.L. Chu, X.Z. Song, Q. Li, Y.R. Li, F. He, X.S. Gu, et al., Basic mechanisms of peripheral nerve injury and treatment via electrical stimulation, Neural Regen Res 17 (10) (2022) 2185–2193, https://doi.org/10.4103/1673-5374.335823.

[31] Z. Wang, Z. Liu, C. Wu, S. Liu, D. Wang, C. Hu, et al., Computational analysis on antioxidant activity of four characteristic structural units from persimmon tannin, Materials 16 (1) (2022), https://doi.org/10.3390/ma16010320.

[32] L. Wang, S. Hu, M.W. Ullah, X. Li, Z. Shi, G. Yang, Enhanced cell proliferation by electrical stimulation based on electroactive regenerated bacterial cellulose hydrogels, Carbohydrate polymers 249 (2020) 116829, https://doi.org/10.1016/j.carbpol.2020.116829.

[33] S. Wang, S. Guan, C. Sun, H. Liu, T. Liu, X. Ma, Electrical stimulation enhances the neuronal differentiation of neural stem cells in three-dimensional conductive scaffolds through the voltage-gated calcium ion channel, Brain Res. 1798 (2023) 148163, https://doi.org/10.1016/j.brainres.2022.148163.

[34] H. Cheng, Y. Huang, H. Yue, Y. Fan, Electrical stimulation promotes stem cell neural differentiation in tissue engineering, Stem Cell. Int. 2021 (2021) 6697574, https://doi.org/10.1155/2021/6697574.

[35] E. Konstantinou, Z. Zagoriti, A. Pyriochou, K. Poulas, Microcurrent stimulation triggers MAPK signaling and TGF-β1 release in fibroblast and osteoblast-like cell lines, Cells 9 (9) (2020), https://doi.org/10.3390/cells9091924.

[36] N.J. Batty, K.K. Fenrich, K. Fouad, The role of cAMP and its downstream targets in neurite growth in the adult nervous system, Neurosci. Lett. 652 (2017) 56–63, https://doi.org/10.1016/j.neulet.2016.12.033.

[37] L. Ayanwuyi, N. Tokarska, N.A. McLean, J.M. Johnston, V.M.K. Verge, Brief electrical nerve stimulation enhances intrinsic repair capacity of the focally demyelinated central nervous system, Neural Regen Res 17 (5) (2022) 1042–1050, https://doi.org/10.4103/1673-5374.324848.

[38] A. Soltani Khaboushan, A. Azimzadeh, S. Behboodi Tanourlouee, M. Mamdoohi, A. M. Kajbafzadeh, K.V. Slavin, et al., Electrical stimulation enhances sciatic nerve regeneration using a silk-based conductive scaffold beyond traditional nerve guide conduits, Sci. Rep. 14 (1) (2024) 15196, https://doi.org/10.1038/s41598-024-65286-9.

[39] J. Kuchinka, C. Willems, D.V. Telyshev, T. Groth, Control of blood coagulation by hemocompatible material surfaces-A review, Bioengineering (Basel, Switzerland) 8 (12) (2021), https://doi.org/10.3390/bioengineering8120215.

[40] M. Weber, H. Steinle, S. Golombek, L. Hann, C. Schlensak, H.P. Wendel, et al., Blood-contacting biomaterials: in vitro evaluation of the hemocompatibility, Front. Bioeng. Biotechnol. 6 (2018) 99, https://doi.org/10.3389/fbioe.2018.00099.

[41] J.P. Robinson, L.H. Bruner, C.F. Bassoe, J.L. Hudson, P.A. Ward, S.H. Phan, Measurement of intracellular fluorescence of human monocytes relative to oxidative metabolism, J. Leukoc. Biol. 43 (4) (1988) 304–310, https://doi.org/10.1002/jlb.43.4.304.

[42] C. Paul, D.M. Brady, Comparative bioavailability and utilization of particular forms of B(12) supplements with potential to mitigate B(12)-related genetic polymorphisms, Integr. Med. 16 (1) (2017) 42–49.

[43] R. An, D. Li, Y. Dong, Q. She, T. Zhou, X. Nie, et al., Methylcobalamin protects melanocytes from H(2)O(2)-induced oxidative stress by activating the Nrf2/HO-1 pathway, Drug Des. Dev. Ther. 15 (2021) 4837–4848, https://doi.org/10.2147/dddt.s336066.

[44] R.G. Daré, C.V. Nakamura, V.F. Ximenes, S.O.S. Lautenschlager, Tannic acid, a promising anti-photoaging agent: evidences of its antioxidant and anti-wrinkle potentials, and its ability to prevent photodamage and MMP-1 expression in L929 fibroblasts exposed to UVB, Free radical biology & medicine 160 (2020) 342–355, https://doi.org/10.1016/j.freeradbiomed.2020.08.019.

[45] Y. Yan, R. Yao, J. Zhao, K. Chen, L. Duan, T. Wang, et al., Implantable nerve guidance conduits: material combinations, multi-functional strategies and advanced engineering innovations, Bioact. Mater. 11 (2022) 57–76, https://doi.org/10.1016/j.bioactmat.2021.09.030.

[46] M.R. Abidian, E.D. Daneshvar, B.M. Egeland, D.R. Kipke, P.S. Cederna, M.G. Urbanchek, Hybrid conducting polymer-hydrogel conduits for axonal growth and neural tissue engineering, Adv. Healthcare Mater. 1 (6) (2012) 762–767, https://doi.org/10.1002/adhm.201200182.

[47] L. Huang, J. Hu, L. Lang, X. Wang, P. Zhang, X. Jing, et al., Synthesis and characterization of electroactive and biodegradable ABA block copolymer of polylactide and aniline pentamer, Biomaterials 28 (10) (2007) 1741–1751, https://doi.org/10.1016/j.biomaterials.2006.12.007.

[48] M.B. Runge, M. Dadsetan, J. Baltrusaitis, A.M. Knight, T. Ruesink, E.A. Lazcano, et al., The development of electrically conductive polycaprolactone fumarate-polypyrrole composite materials for nerve regeneration, Biomaterials 31 (23) (2010) 5916–5926, https://doi.org/10.1016/j.biomaterials.2010.04.012.

[49] Maciel Mangueira M. de Almeida Melo, E. Caparelli-Dáquer, O.P.G. Filho, D. de Assis, J.K.C. Sousa, W.L. Lima, et al., Raman spectroscopy and sciatic functional index (SFI) after low-level laser therapy (LLLT) in a rat sciatic nerve crush injury model, Laser Med. Sci. 37 (7) (2022) 2957–2971, https://doi.org/10.1007/s10103-022-03565-5.

[50] L. Yin, Y. An, X. Chen, H.X. Yan, T. Zhang, X.G. Lu, et al., Local vibration therapy promotes the recovery of nerve function in rats with sciatic nerve injury, Journal of integrative medicine 20 (3) (2022) 265–273, https://doi.org/10.1016/j.joim.2022.02.001.

[51] N.K. Birenbaum, Y. Yan, A. Odabas, N.S. Chandra, W.Z. Ray, M.R. MacEwan, Multiple sessions of therapeutic electrical stimulation using implantable thin-film wireless nerve stimulators improve functional recovery after sciatic nerve isograft repair, Muscle Nerve 67 (3) (2023) 244–251, https://doi.org/10.1002/mus.27776.

[52] J.M. Bin, D. Suminaite, S.K. Benito-Kwiecinski, L. Kegel, M. Rubio-Brotons, J.J. Early, et al., Importin 13-dependent axon diameter growth regulates conduction speeds along myelinated CNS axons, Nat. Commun. 15 (1) (2024) 1790, https://doi.org/10.1038/s41467-024-45908-6.

[53] K.K. Das, B. Basu, P. Maiti, A.K. Dubey, Interplay of piezoelectricity and electrical stimulation in tissue engineering and regenerative medicine, Appl. Mater. Today 39 (2024), https://doi.org/10.1016/j.apmt.2024.102332.

[54] D. Triolo, G. Dina, I. Lorenzetti, M. Malaguti, P. Morana, U. Del Carro, et al., Loss of glial fibrillary acidic protein (GFAP) impairs Schwann cell proliferation and delays nerve regeneration after damage, J. Cell Sci. 119 (Pt 19) (2006) 3981–3993, https://doi.org/10.1242/jcs.03168.

[55] M. Khalil, C.E. Teunissen, S. Lehmann, M. Otto, F. Piehl, T. Ziemssen, et al., Neurofilaments as biomarkers in neurological disorders - towards clinical application, Nat. Rev. Neurol. 20 (5) (2024) 269–287, https://doi.org/10.1038/s41582-024-00955-x.

[56] J. Steiner, H.G. Bernstein, H. Bielau, A. Berndt, R. Brisch, C. Mawrin, et al., Evidence for a wide extra-astrocytic distribution of S100B in human brain, BMC Neurosci. 8 (2007) 2, https://doi.org/10.1186/1471-2202-8-2.

[57] Y. Ukon, T. Makino, J. Kodama, H. Tsukazaki, D. Tateiwa, H. Yoshikawa, et al., Molecular-based treatment strategies for osteoporosis: a literature review, Int. J. Mol. Sci. 20 (10) (2019), https://doi.org/10.3390/ijms20102557.

[58] B. Nyström, Postnatal development of motor nerve terminals in "slow-red" and "fast-white" cat muscles, Acta Neurol. Scand. 44 (3) (1968) 363–383, https://doi.org/10.1111/j.1600-0404.1968.tb05578.x.

[59] K.S. Cramer, D.C. Van Essen, Maturation of fast and slow motor units during synapse elimination in the rabbit soleus muscle, Developmental biology 171 (1) (1995) 16–26, https://doi.org/10.1006/dbio.1995.1256.

[60] R.A. Jones, C. Harrison, S.L. Eaton, M. Llavero Hurtado, L.C. Graham, L. Alkhammash, et al., Cellular and molecular anatomy of the human neuromuscular junction, Cell Rep. 21 (9) (2017) 2348–2356, https://doi.org/10.1016/j.celrep.2017.11.008.

[61] J.N. Sleigh, R.W. Burgess, T.H. Gillingwater, M.Z. Cader, Morphological analysis of neuromuscular junction development and degeneration in rodent lumbrical muscles, J. Neurosci. Methods 227 (2014) 159–165, https://doi.org/10.1016/j.jneumeth.2014.02.005.

[62] J.C. Tapia, J.D. Wylie, N. Kasthuri, K.J. Hayworth, R. Schalek, D.R. Berger, et al., Pervasive synaptic branch removal in the mammalian neuromuscular system at birth, Neuron 74 (5) (2012) 816–829, https://doi.org/10.1016/j.neuron.2012.04.017.

[63] I.W. Smith, M. Mikesh, Y. Lee, W.J. Thompson, Terminal Schwann cells participate in the competition underlying neuromuscular synapse elimination, J. Neurosci. : the official journal of the Society for Neuroscience 33 (45) (2013) 17724–17736, https://doi.org/10.1523/jneurosci.3339-13.2013.

[64] A.M. Mech, A.L. Brown, G. Schiavo, J.N. Sleigh, Morphological variability is greater at developing than mature mouse neuromuscular junctions, J. Anat. 237 (4) (2020) 603–617, https://doi.org/10.1111/joa.13228.

[65] A.C. Missias, G.C. Chu, B.J. Klocke, J.R. Sanes, J.P. Merlie, Maturation of the acetylcholine receptor in skeletal muscle: regulation of the AChR gamma-to-epsilon switch, Developmental biology 179 (1) (1996) 223–238, https://doi.org/10.1006/dbio.1996.0253.

[66] J.J. McArdle, F.M. Sansone, Re-innervation of fast and slow twitch muscle following nerve crush at birth, The Journal of physiology 271 (3) (1977) 567–586, https://doi.org/10.1113/jphysiol.1977.sp012015.

[67] S.J. Wood, C.R. Slater, The contribution of postsynaptic folds to the safety factor for neuromuscular transmission in rat fast- and slow-twitch muscles, The Journal of physiology 500 (Pt 1) (1997) 165–176, https://doi.org/10.1113/jphysiol.1997.sp022007. Pt 1.

[68] S. Schiaffino, C. Reggiani, Fiber types in mammalian skeletal muscles, Physiol. Rev. 91 (4) (2011) 1447–1531, https://doi.org/10.1152/physrev.00031.2010.

[69] J. Talbot, L. Maves, Skeletal muscle fiber type: using insights from muscle developmental biology to dissect targets for susceptibility and resistance to muscle disease, Wiley interdisciplinary reviews Developmental biology 5 (4) (2016) 518–534, https://doi.org/10.1002/wdev.230.

[70] M.A. Alnaqeeb, G. Goldspink, Changes in fibre type, number and diameter in developing and ageing skeletal muscle, J. Anat. 153 (1987) 31–45.

[71] N. Stifani, Motor neurons and the generation of spinal motor neuron diversity, Front. Cell. Neurosci. 8 (2014) 293, https://doi.org/10.3389/fncel.2014.00293.

[72] J. Chen, Y. Zhu, H. Gao, X. Chen, D. Yi, M. Li, et al., HucMSCs delay muscle atrophy after peripheral nerve injury through exosomes by repressing muscle-specific ubiquitin ligases, Stem cells (Dayton, Ohio) 42 (5) (2024) 460–474, https://doi.org/10.1093/stmcls/sxae017.

[73] S. Ciciliot, A.C. Rossi, K.A. Dyar, B. Blaauw, S. Schiaffino, Muscle type and fiber type specificity in muscle wasting, Int. J. Biochem. Cell Biol. 45 (10) (2013) 2191–2199, https://doi.org/10.1016/j.biocel.2013.05.016.

[74] A. Wilden, J. Glaubitz, O. Otto, D. Biedenweg, M. Nauck, M. Mack, et al., Mobilization of CD11b(+)/Ly6c(hi) monocytes causes multi organ dysfunction syndrome in acute pancreatitis, Front. Immunol. 13 (2022) 991295, https://doi.org/10.3389/fimmu.2022.991295.

[75] X. Lu, R. Yu, Z. Li, M. Yang, J. Dai, M. Liu, JC-010a, a novel selective SHP2 allosteric inhibitor, overcomes RTK/non-RTK-mediated drug resistance in multiple oncogene-addicted cancers, Cancer Lett. 582 (2024) 216517, https://doi.org/10.1016/j.canlet.2023.216517.